Comput Mech (2011) 48:97–120
DOI 10.1007/s00466-011-0576-7

ORIGINAL PAPER

Consistent tangent moduli for multi-yield-surface J_2 plasticity model

Q. Gu · J. P. Conte · Z. Yang · A. Elgamal

Received: 13 May 2010 / Accepted: 25 January 2011 / Published online: 4 March 2011

Abstract For problems involving rate constitutive equations, such as rate-independent elasto-plasticity, consistent or algorithmic tangent moduli (operators) play an important role in preserving the asymptotic quadratic rate of convergence of incremental-iterative solution schemes based on Newton's method. Furthermore, consistent (algorithmic) tangent moduli are required in structural response sensitivity analysis based on the direct differentiation method. This paper focuses on the derivation of the consistent tangent moduli for a pressure independent multi-yield-surface J_2 (Von Mises) plasticity model that has been used extensively in nonlinear constitutive modeling of soil materials, but can be used for other materials as well. Application examples are provided to validate the consistent tangent moduli derived herein, and to compare the rate of convergence and computational time of nonlinear incremental-iterative analyses performed using the consistent and continuum tangent moduli, respectively.

Keywords Plasticity-based finite element model · Multi-yield-surface plasticity model · Continuum tangent moduli · Consistent tangent moduli · Incremental-iterative method · Convergence rate

Q. Gu
School of Architecture and Civil Engineering, Xiamen University, Xiamen 361005, Fujian, People's Republic of China
e-mail: quangu@xmu.edu.cn

J. P. Conte (✉) · A. Elgamal
Department of Structural Engineering, University of California at San Diego, La Jolla, CA 92093, USA
e-mail: jpconte@ucsd.edu

A. Elgamal
e-mail: aelgamal@soe.ucsd.edu

Z. Yang
California Department of Transportation (Caltrans), Office of Geotechnical Design West, 111 Grand Ave., Mail Station 16, Oakland, CA 94612, USA
e-mail: yangaaa@gmail.com

1 Introduction

As a general class of nonlinear problems in continuum mechanics, rate-independent elasto-plasticity problems are typically solved through the finite element method (FEM) and using Newton's method. Newton's method is used in conjunction with an incremental-iterative solution procedure which, at each time or load step, reduces the nonlinear problem to a sequence of linearized problems called iterations. Thus, at every iteration, a linearized incremental problem is solved, which requires the tangent stiffness matrix of the structure. In general, this tangent stiffness matrix can be computed from the material tangent moduli (operators) at the material (or integration point) level. In rate-independent plasticity, the material constitutive behavior is described by rate constitutive equations ($\dot{\boldsymbol{\sigma}} = \dot{\boldsymbol{\sigma}}(\dot{\boldsymbol{\varepsilon}})$). The above incremental-iterative process requires these rate constitutive equations to be integrated numerically over a sequence of discrete time or load steps, i.e., $\Delta\boldsymbol{\sigma} = \Delta\boldsymbol{\sigma}(\Delta\boldsymbol{\varepsilon})$. Two types of material tangent moduli can be selected to form the structure stiffness matrix: continuum tangent moduli and consistent tangent moduli. Consistent tangent moduli (also called algorithmic tangent moduli) are obtained through differentiation of the incremental constitutive equations ($\Delta\boldsymbol{\sigma} = \Delta\boldsymbol{\sigma}(\Delta\boldsymbol{\varepsilon})$) with respect to the total incremental strains $\Delta\boldsymbol{\varepsilon}$, while the continuum tangent moduli are defined as the differentiation of the rate constitutive equations ($\dot{\boldsymbol{\sigma}} = \dot{\boldsymbol{\sigma}}(\dot{\boldsymbol{\varepsilon}})$) with respect to the strain rate $\dot{\boldsymbol{\varepsilon}}$ [1]. Previous studies [1,2] show that use

of the consistent tangent moduli guarantees the quadratic rate of asymptotic convergence of Newton's iterative process. Furthermore, for parameter sensitivity analysis in nonlinear mechanics using the direct differentiation method (DDM), the consistent tangent moduli are also required when differentiating the discretized response equations (i.e., static or dynamic equilibrium equations) with respect to material, geometric or loading parameters in order to obtain the governing response sensitivity equations [3–5].

This paper presents the derivation of the consistent tangent moduli for an existing multi-yield-surface J_2 plasticity model. This plasticity model was first developed by Iwan [6] and Mroz [7], and then applied to soil mechanics by Prevost [8–10]. It was later modified and implemented in OpenSees by Elgamal et al. [11] with the tangent stiffness matrix based on the continuum tangent moduli. OpenSees [12] is an open source software framework for advanced modeling and simulation of structural and geotechnical systems developed under the auspice of the Pacific Earthquake Engineering Research (PEER) Center (http://peer.berkeley.edu). In contrast to the classical J_2 (or Von Mises) plasticity model with a single yield surface, the multi-yield-surface J_2 plasticity model employs the concept of a field of plastic moduli [6,7] to achieve a better representation of the material plastic behavior under cyclic loading conditions. This field is defined by a collection of nested yield surfaces of constant size (i.e., no isotropic hardening) in the stress space, which define the regions of constant plastic shear moduli (and constant tangent shear moduli). At each time or load step, it is not possible to know a priori which and how many yield surfaces will be reached (or activated) until convergence (or global equilibrium) is achieved at this step. Hence, the expression of the consistent tangent moduli (or operators) at the current stress point (not necessarily converged at the structure level) depends on all of those yield surfaces that have contributed to the change of stress state from the last converged time or load step. In this paper, a general methodology is presented to compute the consistent tangent moduli by accumulating the contributions from all yield surfaces affecting the stress change from the last converged time/load step to the current stress state.

The work presented in this paper significantly enhances the algorithmic implementation of the existing multi-yield-surface J_2 plasticity model. Although this material model is a rather old model, it remains an effective and robust model to simulate the 3D undrained response of cohesive materials (with elasto-plastic Masing-type behavior) under cyclic and seismic loading conditions [8–23]. This model has been validated experimentally [8,10]. Also, it is operational in the open-source platform OpenSees [12] through which soil–structure-interaction studies may be conducted by a large user community. Thus, the present work improves significantly the computational efficiency of finite element analysis when using this soil model in solving a wide class of geotechnical [19–21] and soil–foundation-structure interaction problems [13,23] in earthquake engineering. In other words, when compared with the classical continuum tangent moduli, the use of the newly developed consistent tangent moduli significantly improves the convergence rate of the Newton process in analyzing FE models that incorporate this material model, especially for tight convergence tolerance and large load/time steps. It is found that in some applications involving this material model, the use of the consistent tangent moduli allows convergence of the iterative solution process which would otherwise not converge when using the continuum tangent moduli. Furthermore, the newly developed consistent tangent moduli can be used directly in finite element response sensitivity analysis based on the DDM for systems modeled using this multi-yield-surface J_2 plasticity model [24]. Considering that the DDM-based response sensitivity algorithm is a major tool for gradient-based optimization methods used in various sub-fields of structural and/or geotechnical engineering such as structural optimization, reliability analysis, system identification, and FE model updating [3,25], the algorithmic enhancement presented in this paper has a clear impact on these sub-fields.

Development of the consistent tangent moduli presented in this paper includes the following novel implementation details that can carry over to other advanced material constitutive models: (1) To the authors' knowledge, in past work, the consistent tangent moduli have been developed for three-dimensional (3D) single surface J_2 plasticity models [1,2] with implicit constitutive law integration schemes. In this paper, the consistent tangent moduli are developed for a general 3D elasto-plastic material constitutive model, in which the multi-yield-surface J_2 plasticity approach is utilized. (2) In this plasticity model, the stress state at the current load/time step is obtained through a non-iterative corrector scheme, which accumulates contributions from all yield surfaces involved, the number of which varies from load/time step to load/time step [24]. Derivation of the consistent tangent moduli requires differentiating the stress tensor with respect to the strain tensor by following exactly the stress computation algorithm. (3) The newly developed consistent tangent moduli consist of an unsymmetrical fourth-order tensor (exhibiting only minor symmetries, $C_{ijkl} = C_{jikl} = C_{ijlk} = C_{jilk}$, but with $C_{ijkl} \neq C_{klij}$), which is different from the corresponding symmetric tensor of continuum tangent moduli. Furthermore, an important contribution of this paper is to document in detail the constitutive law numerical integration scheme for the multi-yield-surface J_2 plasticity model considered here. Derivation of the flow rule in discrete form is presented in Appendix A, and to the authors' knowledge does not appear anywhere else in the literature. The concepts used in this paper to derive the consistent tangent moduli can be applied to other multi-yield-surface plasticity models defined in the literature [15].

The algorithm derived herein to compute the consistent tangent moduli of the multi-yield-surface J_2 soil plasticity model is then implemented in OpenSees [12]. Application examples are presented to verify the quadratic rate of asymptotic convergence of Newton's iterative process obtained when using the derived consistent tangent moduli. Based on these examples, the convergence rate and computational time obtained when using consistent and continuum tangent moduli are compared.

Implicit integration schemes of other multi-surface plasticity models with derivation of the algorithmic/consistent tangent moduli have been presented by several authors [26–28].

2 Continuum and discrete formulations of multi-yield-surface J_2 plasticity constitutive model

In this section, the constitutive model of the multi-yield-surface J_2 plasticity material is presented in detail. It is worthy to note that in the published literature [8–10,14,15,29], only the mathematical expression of the yield surfaces and the flow in continuum form are clearly explained, i.e., Eqs. (1)–(7). The employed hardening rule was described initially in [11,30] by Elgamal and co-workers. A complete presentation of the flow rule in discrete form, Eqs. (8)–(20), is not presented elsewhere. Furthermore, the plastic stress correction tensor used in the discretized flow rule is derived independently by the authors and after some simplifications and approximations (see Appendix A) reduces to the same form as the one given by Parra [30] and Yang [14] and implemented in OpenSees [12]. The discrete form of the constitutive model is essential in this paper, since it represents the starting point to derive the consistent (or algorithmic) tangent moduli.

2.1 Multi-yield surfaces

Each yield surface of this multi-yield-surface J_2 plasticity model is defined in the deviatoric stress space as

$$f = \left\{ \frac{3}{2} (\boldsymbol{\tau} - \boldsymbol{\alpha}) : (\boldsymbol{\tau} - \boldsymbol{\alpha}) \right\}^{\frac{1}{2}} - K = 0 \tag{1}$$

where $\boldsymbol{\tau}$ denotes the deviatoric stress tensor and $\boldsymbol{\alpha}$, referred to as back-stress tensor, denotes the center of the yield surface $\{f = 0\}$ in the deviatoric stress space. Parameter K represents the size ($\sqrt{3/2}$ times the radius) of the yield surface which defines the region of constant plastic shear moduli. The dyadic tensor product of tensors $\mathbf{A}$ and $\mathbf{B}$ is defined as $\mathbf{A} : \mathbf{B} = A_{ij} B_{ij}$. The back-stress $\boldsymbol{\alpha}$ is initialized to zero at the start of loading.

In geotechnical engineering, soil nonlinear shear behavior is described by a shear stress–strain backbone curve [31] as shown in Fig. 1a. The experimentally determined backbone curve can be approximated by the hyperbolic formula [32] as

$$\tau = \frac{G\gamma}{1 + \gamma/\gamma_r} \tag{2}$$

where $\boldsymbol{\tau}$ and γ denote the octahedral shear stress and shear strain, respectively, and G is the low-strain shear modulus. Parameter γ_r is a reference shear strain defined as

$$\gamma_r = \frac{\gamma_{max} \cdot \tau_{max}}{G \cdot \gamma_{max} - \tau_{max}} \tag{3}$$

where τ_{max}, called shear strength, is the shear stress corresponding to the shear strain $\gamma = \gamma_{max}$ (selected sufficiently large so that $\tau_{max} \approx \tau(\gamma = \infty)$ (Fig. 1).

Within the framework of multi-yield-surface plasticity, the hyperbolic backbone curve in Eq. (2) is replaced by a piecewise linear approximation as shown in Fig. 1a. Each line segment represents the domain of a yield surface $\{f_i = 0\}$ of size K_i characterized by an elasto-plastic shear modulus $H^{(i)}$ for $i = 1, 2, \ldots,$ NYS, where NYS denotes the total number of yield surfaces [8–10]. Parameter $H^{(i)}$ is conveniently defined as $H^{(i)} = 2\left(\frac{\tau_{i+1} - \tau_i}{\gamma_{i+1} - \gamma_i}\right)$ [33].

2.2 Flow rule (continuum form)

A constant plastic shear modulus $H'^{(i)}$ defined as

$$\frac{1}{H'^{(i)}} = \frac{1}{H^{(i)}} - \frac{1}{2G} \tag{4}$$

is associated with each yield surface $\{f_i = 0\}$. The plastic shear modulus associated with the outermost yield surface is set to zero, i.e., $H'^{(NYS)} = 0$. An associative flow rule is used to compute the plastic strain increments. In the deviatoric stress space, the plastic strain increment vector lies along the exterior normal to the yield surface at the stress point. In tensor notation, the plastic strain increment is expressed as

$$d\boldsymbol{\varepsilon}^p = \frac{\langle L \rangle}{H'} \mathbf{Q} \tag{5}$$

where the second-order unit tensor $\mathbf{Q}$ defined as

$$\mathbf{Q} = \frac{1}{Q} \frac{\partial f}{\partial \sigma} \tag{6}$$

in which $Q = \left\{ \frac{\partial f}{\partial \sigma} : \frac{\partial f}{\partial \sigma} \right\}^{\frac{1}{2}}$, represents the plastic flow direction normal to the yield surface $\{f = 0\}$ at the current stress point. Parameter L in Eq. (5), referred to as the plastic loading function, is defined as the projection of the stress increment vector $d\boldsymbol{\tau}$ onto the direction normal to the yield surface, i.e.,

$$L = \mathbf{Q} : d\boldsymbol{\tau} \tag{7}$$

The symbol $\langle\rangle$ in Eq. (5) denotes the MacCauley's brackets defined such that $\langle L \rangle = \max(L, 0)$. The magnitude of the plastic strain increment, $\frac{\langle L \rangle}{H'}$, is a non-negative function (from Eq. (5) and the definition of McCauley's brackets) which is

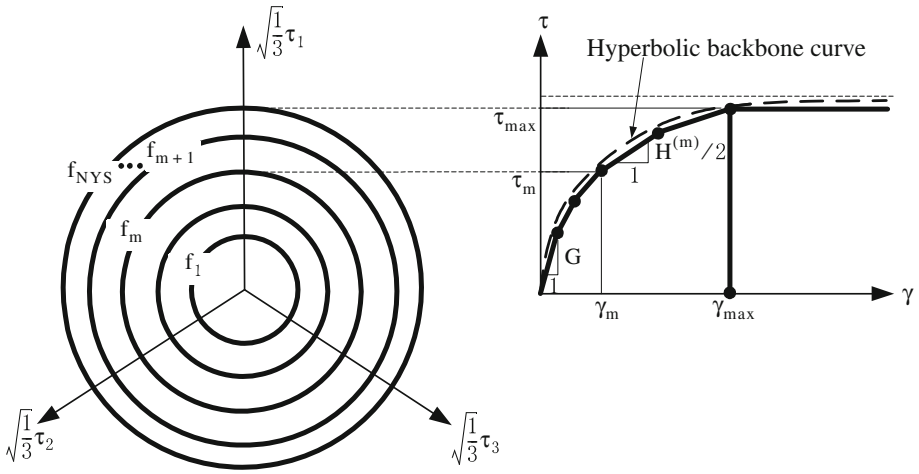

(a) Octahedral shear stress-strain

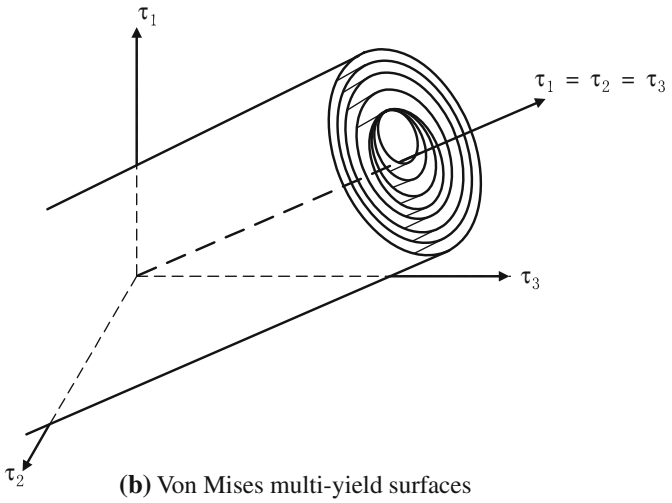

(b) Von Mises multi-yield surfaces

Fig. 1 Yield surfaces of multi-yield-surface J_2 plasticity model in principal deviatoric stress space after [8,18]

assumed to obey the Kuhn–Tucker complementarity conditions expressed as $\frac{\langle L \rangle}{H'} f(\boldsymbol{\tau}, \boldsymbol{\alpha}) = 0$, such that the plastic strain increment is zero in the elastic case (i.e., when $f(\boldsymbol{\tau}, \boldsymbol{\alpha}) < 0$).

2.3 Discretized form of flow rule

The flow rule defined above in differential (continuum) form is integrated numerically over a trial time step (or load step) using an elastic predictor-plastic corrector procedure illustrated in Fig. 2, which shows, as an illustration, two corrective iterations before convergence is achieved. In this figure, subscript i is attached to the parameters and quantities related to the *i*th corrective iteration. Assuming that the current active yield surface is $\{f_m = 0\}$ with its center at $\boldsymbol{\alpha}^{(m)}$, the elastic trial (deviatoric) stress $\boldsymbol{\tau}_0^{tr}$ is obtained as

$$\boldsymbol{\tau}_0^{tr} = \boldsymbol{\tau}_n + 2G \cdot \Delta \mathbf{e} \tag{8}$$

where $\boldsymbol{\tau}_n$ is the converged deviatoric stress at the last (*n*th) time step, and $\Delta \mathbf{e}$ denotes the total (from last converged step) deviatoric strain increment in the current time step. If the trial stress $\boldsymbol{\tau}_0^{tr}$ falls inside the current yield surface $\{f_m = 0\}$, then the iteration process for the integration of the material constitutive law is converged, otherwise a plastic correction is applied as follows. The contact stress $\boldsymbol{\tau}_1^*$, defined as the intersection point of vector $\boldsymbol{\tau}_0^{tr} - \boldsymbol{\alpha}^{(m)}$ and the current active yield surface $\{f_m = 0\}$, can be computed as (Fig. 2)

$$\boldsymbol{\tau}_1^* = \frac{K^{(m)}}{K_1}\left(\boldsymbol{\tau}_0^{tr} - \boldsymbol{\alpha}^{(m)}\right) + \boldsymbol{\alpha}^{(m)} \tag{9}$$

where K_1 is defined as

$$K_1 = \sqrt{\frac{3}{2}\left(\boldsymbol{\tau}_0^{tr} - \boldsymbol{\alpha}^{(m)}\right) : \left(\boldsymbol{\tau}_0^{tr} - \boldsymbol{\alpha}^{(m)}\right)} \tag{10}$$

which is $\sqrt{3/2}$ times the distance from $\boldsymbol{\tau}_0^{tr}$ to $\boldsymbol{\alpha}^{(m)}$.

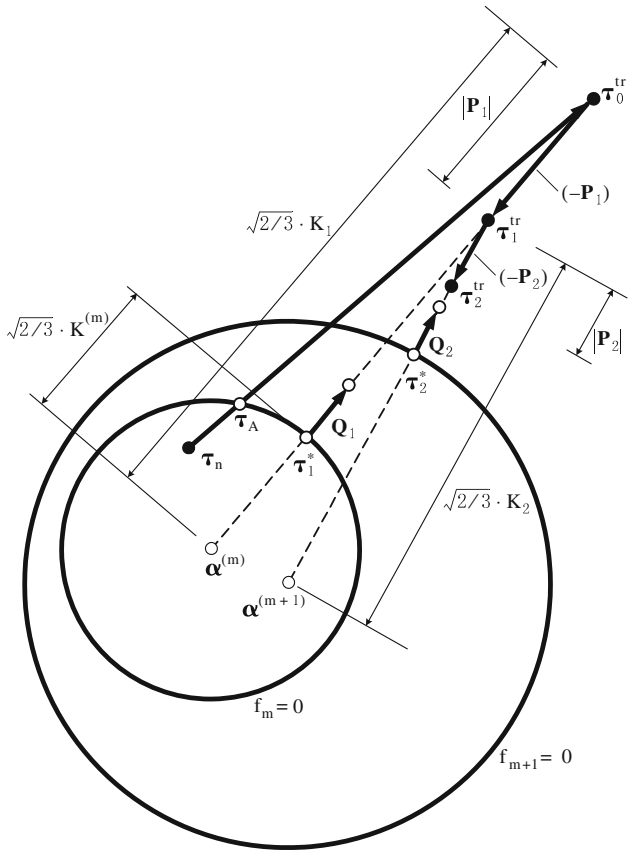

Fig. 2 Flow rule of multi-yield-surface J_2 plasticity model

The vector normal to the yield surface at $\boldsymbol{\tau}_1^*$ is derived from Eq. (6) or Fig. 2 as

$$\mathbf{Q}_1 = \frac{\left(\boldsymbol{\tau}_1^* - \boldsymbol{\alpha}^{(m)}\right)}{\sqrt{\left(\boldsymbol{\tau}_1^* - \boldsymbol{\alpha}^{(m)}\right) : \left(\boldsymbol{\tau}_1^* - \boldsymbol{\alpha}^{(m)}\right)}} \tag{11}$$

The plastic stress correction tensor is defined as

$$\mathbf{P}_1 = \boldsymbol{\tau}_0^{tr} - \boldsymbol{\tau}_1^{tr} \tag{12}$$

where the plastic stress correction tensor $\mathbf{P}_1$ can be expressed as [14,34] (see Appendix A)

$$\mathbf{P}_1 = 2G\frac{\mathbf{Q}_1 : \left(\boldsymbol{\tau}_0^{tr} - \boldsymbol{\tau}_1^*\right)}{\left(H'^{(m)} + 2G\right)}\mathbf{Q}_1 \tag{13}$$

Then, the trial stress after the first plastic correction for the current active yield surface$\{f_m = 0\}$ becomes

$$\boldsymbol{\tau}_1^{tr} = \boldsymbol{\tau}_0^{tr} - \mathbf{P}_1 \tag{14}$$

If the trial stress $\boldsymbol{\tau}_1^{tr}$ lies outside the next yield surface $\{f_{m+1} = 0\}$, the subscript for the iteration number is set to $i = 2$, and the above plastic correction process is repeated with some modifications. For the iterations $i = 2, 3, \ldots$ (corresponding to the number of the active surface $m + 1, m + 2, \ldots$, respectively), Eqs. (9)–(14) are replaced by Eqs. (15)–(20) below, with the iterations continued until the trial stress $\boldsymbol{\tau}_i^{tr}$ falls inside the yield surface $\{f_{m+i} = 0\}$. The derivation of Eq. (19) is provided in Appendix A.

$$\boldsymbol{\tau}_i^* = \frac{K^{(m+i-1)}}{K_i}\left(\boldsymbol{\tau}_{i-1}^{tr} - \boldsymbol{\alpha}^{(m+i-1)}\right) + \boldsymbol{\alpha}^{(m+i-1)} \tag{15}$$

$$K_i = \sqrt{\frac{3}{2}\left(\boldsymbol{\tau}_{i-1}^{tr} - \boldsymbol{\alpha}^{(m+i-1)}\right) : \left(\boldsymbol{\tau}_{i-1}^{tr} - \boldsymbol{\alpha}^{(m+i-1)}\right)} \tag{16}$$

$$\mathbf{Q}_i = \frac{\left(\boldsymbol{\tau}_i^* - \boldsymbol{\alpha}^{(m+i-1)}\right)}{\sqrt{\left(\boldsymbol{\tau}_i^* - \boldsymbol{\alpha}^{(m+i-1)}\right) : \left(\boldsymbol{\tau}_i^* - \boldsymbol{\alpha}^{(m+i-1)}\right)}} \tag{17}$$

$$\mathbf{P}_i = \boldsymbol{\tau}_{i-1}^{tr} - \boldsymbol{\tau}_i^{tr} \tag{18}$$

$$\mathbf{P}_i = 2G\,\frac{\mathbf{Q}_i : \left(\boldsymbol{\tau}_{i-1}^{tr} - \tau_i^*\right)}{\left(H'^{(m+i-1)} + 2G\right)}\,\frac{\left(H'^{(m+i-2)} - H'^{(m+i-1)}\right)}{H'^{(m+i-2)}}\,\mathbf{Q}_i \tag{19}$$

$$\boldsymbol{\tau}_i^{tr} = \boldsymbol{\tau}_{i-1}^{tr} - \mathbf{P}_i \tag{20}$$

After "convergence" of the deviatoric stress $\boldsymbol{\tau}_i^{tr}$ to $\boldsymbol{\tau}$ (referred to as the current stress herein) is achieved following the above iterative algorithm, the active yield surface index is updated to $m = m + i - 1$, and the volumetric stress σ^{vol} is updated to

$$\sigma^{vol} = \sigma_n^{vol} + B(\Delta\boldsymbol{\varepsilon} : \mathbf{I}) \tag{21}$$

where B = elastic bulk modulus, $\Delta\boldsymbol{\varepsilon}$ = total strain tensor increment, and $\mathbf{I}$ = second order unit tensor. Then, the new total stress (at the end of the integration of the material constitutive law over a trial time/load step) referred to as the current stress point is given by

$$\boldsymbol{\sigma} = \boldsymbol{\tau} + \sigma^{vol}\mathbf{I} \tag{22}$$

2.4 Hardening Law (both continuum and discretized forms)

A pure deviatoric kinematic hardening rule is employed to capture the hysteretic cyclic response behavior of real materials such as cohesionless soils [11]. Accordingly, all yield surfaces may translate in the deviatoric stress space to the current stress point without changing in form (i.e., no isotropic hardening). In the context of multi-yield-surface plasticity, translation of the current active yield surface $\{f_m = 0\}$ is generally governed by the consideration that no overlapping is allowed between the current and next yield surfaces. The translation direction $\boldsymbol{\mu}$ as shown in Fig. 3 is defined as [11]

$$\boldsymbol{\mu} = \left(\boldsymbol{\tau}_T - \boldsymbol{\alpha}^{(m)}\right) - \frac{K^{(m)}}{K^{(m+1)}}\left(\boldsymbol{\tau}_T - \boldsymbol{\alpha}^{(m+1)}\right) \tag{23}$$

where $\boldsymbol{\tau}_T$is the deviatoric stress tensor defining the position of stress point T, see Fig. 3, as the intersection of $\{f_{m+1} = 0\}$ (the yield surface next to the current active yield surface) with the vector connecting the center $\boldsymbol{\alpha}^{(m)}$ of the current yield surface and the current stress state ($\boldsymbol{\tau}$) at the end of the trial time/load step. The hardening rule defined in Eq. (23) is also

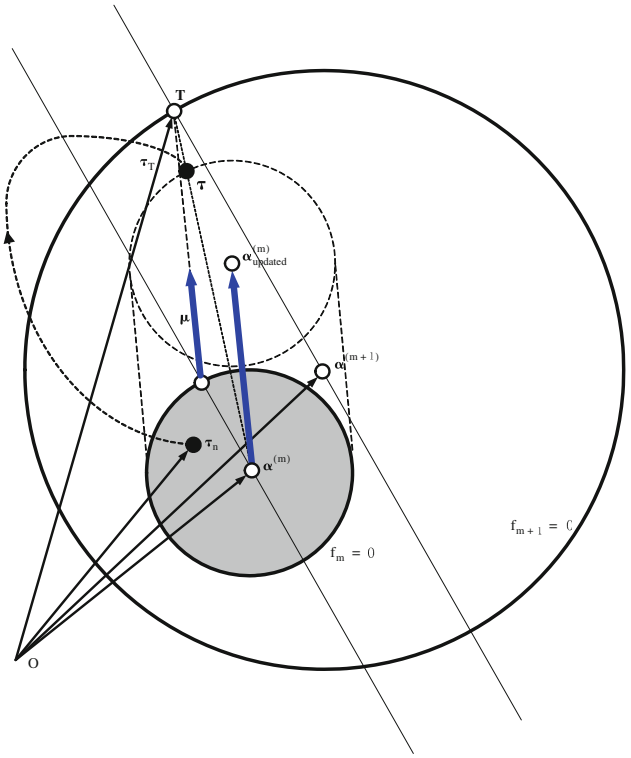

Fig. 3 Hardening rule of multi-yield-surface J_2 plasticity model (where $\{f_m = 0\}$ represents the current active yield surface, τ_n is the converged deviatoric stress at the last time step, and is the current stress at the end of the trial time/load step) after [11]

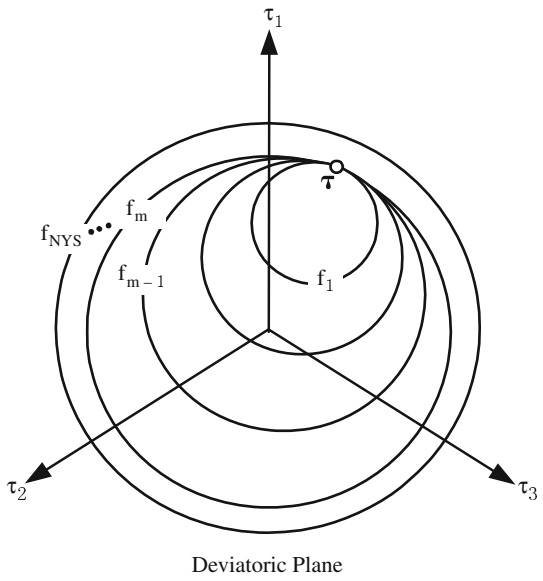

Fig. 4 Inner yield surface movements after [8,18]

based on Mroz conjugate-points concept [7], and guarantees no overlapping of yield surfaces [11]. Once the translation direction $\boldsymbol{\mu}$ is computed from Eq. (23), the current active yield surface $\{f_m = 0\}$ is translated in the direction $\boldsymbol{\mu}$ until it touches the current stress point $\boldsymbol{\tau}$.

After the current active yield surface $\{f_m = 0\}$ is updated, all the inner yield surfaces $\{f_1 = 0\}, \{f_2 = 0\}, \ldots, \{f_{m-1} = 0\}$ are updated such that all yield surfaces $\{f_1 = 0\}$ to $\{f_m = 0\}$ are tangent to each other at the current stress point $\boldsymbol{\tau}$ as shown in Fig. 4, which is achieved from similarity as [10]

$$\frac{\left(\boldsymbol{\tau} - \boldsymbol{\alpha}^{(m)}\right)}{K^{(m)}} = \frac{\left(\boldsymbol{\tau} - \boldsymbol{\alpha}^{(m-1)}\right)}{K^{(m-1)}} = \cdots = \frac{\left(\boldsymbol{\tau} - \boldsymbol{\alpha}^{(1)}\right)}{K^{(1)}} \tag{24}$$

Equations (24) are solved for $\boldsymbol{\alpha}^{(k)}$ $(k = 1, 2, \ldots m-1)$ given $\boldsymbol{\alpha}^{(m)}$. The above hardening law controls the movement of the inner yield surfaces.

It is worth mentioning that the hardening law of the constitutive model considered here is defined only in discrete form by Eqs. (23) and (24). No continuum form was defined by the developers of the model for the evolution equations of the back stress α (i.e., strain hardening law). The hardening law for α is based on the assumption that the smooth shear stress–strain backbone curve (which is part of the hardening law) has already been piecewise linearly approximated (i.e., discretized), otherwise Eqs. (23) and (24) do not hold. The validation of the hardening law for α is out of the scope of this paper and the evolution equations for α are not given in detail herein, but can be found elsewhere [24] for the magnitude of the movement of α.

3 Continuum tangent operator

The continuum elastoplastic tangent moduli are obtained through differentiation with respect to $d\boldsymbol{\varepsilon}$ of the rate constitutive equation $d\boldsymbol{\sigma} = d\boldsymbol{\sigma}(d\boldsymbol{\varepsilon})$. where $d\boldsymbol{\sigma}$ and $d\boldsymbol{\varepsilon}$ denote infinitesimal increments in total stress and strain, respectively. In small strain plasticity, the decomposition of the total strain into the elastic and plastic parts can be expressed in infinitesimal form as

$$d\boldsymbol{\varepsilon} = d\boldsymbol{\varepsilon}^{e} + d\boldsymbol{\varepsilon}^{p} \tag{25}$$

where $d\boldsymbol{\varepsilon}^{e}$ and $d\boldsymbol{\varepsilon}^{e}$ denote infinitesimal increments of elastic and plastic (irreversible) strains, respectively. The constitutive equation is based on the relationship between the stress and the elastic strain, namely

$$d\boldsymbol{\sigma} = \mathbf{C} : d\boldsymbol{\varepsilon}^{e} = \mathbf{C} : \left(d\boldsymbol{\varepsilon} - d\boldsymbol{\varepsilon}^{p}\right) = \mathbf{C}^{ep} : d\boldsymbol{\varepsilon} \tag{26}$$

where $\mathbf{C}$ denotes the tensor of elastic moduli, which in the case of isotropic elasticity can be expressed as $C_{ijkl} = \lambda\delta_{ij}\delta_{kl} + \mu(\delta_{ik}\delta_{jl} + \delta_{il}\delta_{jk})$ where λ and μ are Lamé constants, and $\mathbf{C}^{ep}$ represents the tensor of continuum elasto-plastic tangent moduli. Note that Lamé constant μ is identical to the low-strain shear modulus G. In multi-yield-surface J_2 plasticity, the tensor of continuum elasto-plastic tangent moduli

can be obtained as [15]

$$\mathbf{C}^{ep} = \mathbf{C} - \frac{1}{H}\mathbf{H} \otimes \mathbf{H} \tag{27}$$

where the tensor product of two tensors $\mathbf{A}$ and $\mathbf{B}$ is defined as $[\mathbf{A} \otimes \mathbf{B}]_{ijkl} = A_{ij}B_{kl}$ and

$$H = (12G + 6H'^{(m)})\left(K^{(m)}\right)^2 \quad \mathbf{H} = 6G\left(\boldsymbol{\tau} - \boldsymbol{\alpha}^{(m)}\right) \tag{28}$$

4 Derivation of consistent tangent moduli

Consistent tangent moduli were first introduced by Taylor and Simo [1,2]. These moduli are obtained by differentiating directly the discretized constitutive equation $\Delta\boldsymbol{\sigma} = \Delta\boldsymbol{\sigma}(\Delta\boldsymbol{\varepsilon})$ with respect to the strain increment $\Delta\boldsymbol{\varepsilon}$. This ensures that the tangent operator is 'consistent' with the constitutive law integration scheme, which guarantees the quadratic rate of asymptotic convergence of iterative solution strategies (at the structure level) based on Newton's method. The consistent tangent moduli (also called algorithmic tangent moduli in the literature) are defined at a material point as

$$\mathbf{C}^{ep}_{n+1} = \left.\frac{\partial\boldsymbol{\sigma}\left(\boldsymbol{\sigma}_n, \boldsymbol{\varepsilon}_n, \boldsymbol{\varepsilon}^p_n \ldots, \boldsymbol{\varepsilon} - \boldsymbol{\varepsilon}_n\right)}{\partial\boldsymbol{\varepsilon}}\right|_{\boldsymbol{\varepsilon}=\boldsymbol{\varepsilon}_{n+1}} \tag{29}$$

where $\boldsymbol{\sigma}(\boldsymbol{\sigma}_n, \boldsymbol{\varepsilon}_n, \boldsymbol{\varepsilon}^p_n \ldots, \boldsymbol{\varepsilon} - \boldsymbol{\varepsilon}_n)$ denotes the incremental material response function, and the notation $f|_{\boldsymbol{\varepsilon}=\boldsymbol{\varepsilon}_{n+1}}$ indicates that the tensor function f is evaluated at $\boldsymbol{\varepsilon} = \boldsymbol{\varepsilon}_{n+1}$. It is worth mentioning that the stress $\boldsymbol{\sigma}$ is not necessarily the converged one at the structure level at the end of the current trial time step, i.e., it could be the stress at the end of a non-converged iteration at the structure level. The material consistent tangent moduli enable to form the consistent tangent stiffness matrix at both the element and structure levels.

It is important to mention that the consistent tangent moduli are derived analytically from the constitutive law numerical integration scheme. Although they can be verified (which was done extensively during the debugging process) or approximated by using numerical differentiation, the analytically derived consistent tangent moduli cannot be replaced by their approximation obtained through numerical differentiation for the following reasons:

1. The solution obtained from numerical differentiation is subjected to numerical noise. Large perturbations of the various strain components yield large truncation errors in the finite difference approximated consistent tangent moduli, while very small perturbations of the strain components give rise to large round-off errors. It is not easy (if not impossible) to estimate the optimum strain perturbation size in order to minimize the total numerical error (sum of truncation and round-off errors). In some cases, there may not be any strain perturbation size which yields accurate approximations of the consistent tangent moduli. This issue is referred to as "step-size dilemma" in structural optimization [35]. Furthermore, only the analytically derived consistent tangent moduli guarantee the asymptotic rate of quadratic convergence of the Newton iterative process.
2. Estimation by finite difference of the consistent tangent moduli at each numerical integration (Gauss) point is computationally very expensive (in addition of being inaccurate) as compared to the direct evaluation of the analytically derived consistent tangent moduli. At each numerical integration point, it requires perturbing six strain components, one at a time, and computing the resulting increments in the six stress components.
3. Finite element response sensitivity analysis based on the DDM requires the analytically derived consistent tangent moduli.

In this section, which represents the heart of this paper, the consistent tangent moduli are derived for the multi-yield-surface J_2 plasticity material model defined above based on the algorithmic stress updating process defined in Eqs. (8) through (22).

1. *Differentiation of the elastic trial deviatoric stress with respect to the current deviatoric strain*. From Eq. (8), it follows that

$$\frac{\partial\boldsymbol{\tau}^{tr}_0}{\partial\mathbf{e}_{n+1}} = 2G \cdot \mathbf{I}_4 \tag{30}$$

where the derivative of tensor $\mathbf{A}$ with respect to tensor $\mathbf{B}$ is defined as $\frac{\partial\mathbf{A}}{\partial\mathbf{B}} = \frac{\partial A_{ij}}{\partial B_{kl}}\hat{\mathbf{e}}_i \otimes \hat{\mathbf{e}}_j \otimes \hat{\mathbf{e}}_k \otimes \hat{\mathbf{e}}_l$ in which $\hat{\mathbf{e}}_i$ denotes the unit (base) vector along the ith axis, and the 4th order symmetric unit tensor $\mathbf{I}_4$ is defined as $\mathbf{I}_4 = \frac{1}{2}(\delta_{il}\delta_{jk} + \delta_{ik}\delta_{jl})\hat{\mathbf{e}}_i \otimes \hat{\mathbf{e}}_j \otimes \hat{\mathbf{e}}_k \otimes \hat{\mathbf{e}}_l$

2. *Differentiation of the contact stress with respect to the current deviatoric strain*. Differentiating Eqs. (16) and (15) with respect to $\mathbf{e}_{n+1}$ yields

$$\frac{\partial K_i}{\partial\mathbf{e}_{n+1}} = \frac{3}{2K_i}\left(\tau^{tr}_{i-1} - \boldsymbol{\alpha}^{(m+i-1)}\right) : \frac{\partial\boldsymbol{\tau}^{tr}_{i-1}}{\partial\mathbf{e}_{n+1}} \tag{31}$$

$$\frac{\partial\boldsymbol{\tau}^*_i}{\partial\mathbf{e}_{n+1}} = \frac{K^{(m+i-1)}}{K_i} \cdot \frac{\partial\boldsymbol{\tau}^{tr}_{i-1}}{\partial\mathbf{e}_{n+1}} - \frac{K^{(m+i-1)}}{K_i^2}\left(\boldsymbol{\tau}^{tr}_{i-1} - \alpha^{(m+i-1)}\right) \otimes \frac{\partial K_i}{\partial\mathbf{e}_{n+1}} \quad (i = 1, 2, \ldots) \tag{32}$$

3. *Differentiation of the unit vector normal to the yield surface with respect to the current deviatoric strain*.

Differentiating Eq. (17) with respect to $\mathbf{e}_{n+1}$ gives

$$\frac{\partial \mathbf{Q}_i}{\partial \mathbf{e}_{n+1}} = \frac{1}{\sqrt{\left(\boldsymbol{\tau}_i^* - \boldsymbol{\alpha}^{(m+i-1)}\right) : \left(\boldsymbol{\tau}_i^* - \boldsymbol{\alpha}^{(m+i-1)}\right)}} \cdot \frac{\partial \boldsymbol{\tau}_i^*}{\partial \mathbf{e}_{n+1}} - \frac{1}{\sqrt{\left[\left(\boldsymbol{\tau}_i^* - \boldsymbol{\alpha}^{(m+i-1)}\right) : \left(\boldsymbol{\tau}_i^* - \boldsymbol{\alpha}^{(m+i-1)}\right)\right]^3}} \cdot \left(\boldsymbol{\tau}_i^* - \boldsymbol{\alpha}^{(m+i-1)}\right) \otimes \left(\boldsymbol{\tau}_i^* - \alpha^{(m+i-1)}\right) : \frac{\partial \tau_i^*}{\partial \mathbf{e}_{n+1}} \quad (i = 1, 2, \ldots) \tag{33}$$

4. *Differentiation of the plastic stress correction tensor with respect to the current deviatoric strain*. From Eqs. (13) and (19), it follows that

$$\frac{d\mathbf{P}_1}{d\mathbf{e}_{n+1}} = \frac{2G}{\left(H'^{(m)} + 2G\right)}\mathbf{Q}_1 \otimes \left(\left(\boldsymbol{\tau}_0^{tr} - \tau_1^*\right) : \frac{\partial \mathbf{Q}_1}{\partial \mathbf{e}_{n+1}} + \mathbf{Q}_1 : \left(\frac{\partial \boldsymbol{\tau}_0^{tr}}{\partial \mathbf{e}_{n+1}} - \frac{\partial \boldsymbol{\tau}_1^*}{\partial \mathbf{e}_{n+1}}\right)\right) + 2G\frac{\mathbf{Q}_1 : \left(\tau_0^{tr} - \tau_1^*\right)}{\left(H'^{(m)} + 2G\right)} \cdot \frac{\partial \mathbf{Q}_1}{\partial \mathbf{e}_{n+1}} \tag{34}$$

for the first iteration (i = 1)

$$\frac{d\mathbf{P}_i}{d\mathbf{e}_{n+1}} = \frac{2G}{\left(H'^{(m+i-1)}+2G\right)} \frac{\left(H'^{(m+i-2)} - H'^{(m+i-1)}\right)}{H'^{(m+i-2)}}\mathbf{Q}_i \otimes \left(\left(\boldsymbol{\tau}_{i-1}^{tr} - \boldsymbol{\tau}_i^*\right) : \frac{\partial \mathbf{Q}_i}{\partial \mathbf{e}_{n+1}} + \mathbf{Q}_i : \left(\frac{\partial \boldsymbol{\tau}_{i-1}^{tr}}{\partial \mathbf{e}_{n+1}} - \frac{\partial \boldsymbol{\tau}_i^*}{\partial \mathbf{e}_{n+1}}\right)\right) + 2G\frac{\mathbf{Q}_i : \left(\boldsymbol{\tau}_{i-1}^{tr} - \boldsymbol{\tau}_i^*\right)}{\left(H'^{(m+i-1)}+2G\right)} \frac{\left(H'^{(m+i-2)} - H'^{(m+i-1)}\right)}{H'^{(m+i-2)}} \times \frac{\partial \mathbf{Q}_i}{\partial \mathbf{e}_{n+1}} \tag{35}$$

and for subsequent iterations (i = 2, 3, ...)

5. *Differentiation of the new trial stress after plastic correction with respect to the current deviatoric strain.* Differentiating Eq. (20) with respect to $\mathbf{e}_{n+1}$ gives

$$\frac{d\boldsymbol{\tau}_i^{tr}}{d\mathbf{e}_{n+1}} = \frac{\partial \boldsymbol{\tau}_{i-1}^{tr}}{\partial \mathbf{e}_{n+1}} - \frac{d\mathbf{P}_i}{d\mathbf{e}_{n+1}} \quad (i = 1, 2, \ldots) \tag{36}$$

The derivative computations in steps 2 to 5 are repeated until the trial stress $\boldsymbol{\tau}_i^{tr}$ falls inside the yield surface $\{f_{m+i} = 0\}$.

After "convergence" of the deviatoric stress $\boldsymbol{\tau}_i^{tr}$ to $\boldsymbol{\tau}$ at the end of the trial time/load step, the material consistent (or algorithmic) tangent moduli are finally obtained as the differentiation of the current (total) stress σ with respect to the current (total) strain $\boldsymbol{\varepsilon}_{n+1}$, see Eq. (29), as shown below. From the relation between the deviatoric strain tensor $\mathbf{e}_{n+1}$ and total strain tensor $\boldsymbol{\varepsilon}_{n+1}$, i.e., $\mathbf{e}_{n+1} = \boldsymbol{\varepsilon}_{n+1} - \frac{1}{3}(\boldsymbol{\varepsilon} : \mathbf{I})\mathbf{I}$, it follows that

$$\frac{d\mathbf{e}_{n+1}}{d\boldsymbol{\varepsilon}_{n+1}} = \mathbf{I}_4 - \frac{1}{3}\mathbf{I} \otimes \mathbf{I} \tag{37}$$

Then, the differentiation of the current stress $\boldsymbol{\tau}$ with respect to the total strain $\boldsymbol{\varepsilon}_{n+1}$ can be expressed as, using the chain rule of differentiation and Eq. (37),

$$\frac{\partial \boldsymbol{\tau}}{\partial \boldsymbol{\varepsilon}_{n+1}} = \frac{\partial \boldsymbol{\tau}}{\partial \mathbf{e}_{n+1}} : \frac{d\mathbf{e}_{n+1}}{d\boldsymbol{\varepsilon}_{n+1}} = \frac{\partial \boldsymbol{\tau}}{\partial \mathbf{e}_{n+1}} : \left(\mathbf{I}_4 - \frac{1}{3}\mathbf{I} \otimes \mathbf{I}\right) = \frac{\partial \boldsymbol{\tau}}{\partial \mathbf{e}_{n+1}} - \frac{1}{3}\left(\frac{\partial \boldsymbol{\tau}}{\partial \mathbf{e}_{n+1}} : \mathbf{I}\right) \otimes \mathbf{I} \tag{38}$$

The relation between the total stress and deviatoric stress tensors given in Eq. (22) can be re-written as $\boldsymbol{\sigma} = \boldsymbol{\tau} + \sigma^{vol}\mathbf{I} = \boldsymbol{\tau} + B\,(\boldsymbol{\varepsilon} : \mathbf{I})\,\mathbf{I}$. Then

$$\frac{\partial \boldsymbol{\sigma}}{\partial \boldsymbol{\varepsilon}_{n+1}} = \frac{\partial \boldsymbol{\tau}}{\partial \boldsymbol{\varepsilon}_{n+1}} + B\,(\mathbf{I} \otimes \mathbf{I}) \tag{39}$$

The material consistent tangent moduli given in Eq. (39) depend on the sensitivities (with respect to the current strain tensor $\boldsymbol{\varepsilon}_{n+1}$) of all trial stresses $\boldsymbol{\tau}_i^{tr}$ (i = 0, 1, 2, ...) yielding to the current stress state $\boldsymbol{\sigma}$, according to the incremental process defined by Eqs. (30) through (36) or steps 1 through 5. Thus, in the case of multi-yield-surface plasticity, the consistent tangent moduli cannot be evaluated directly from a single expression, but need to be computed in an incremental/additive manner.

The above results for the material consistent tangent moduli, derived in tensor notation, need to be converted into matrix and vector notation for software implementation purposes. In this paper, the 2nd order and 4th order tensors are represented as vectors and matrices, respectively, as

$$\boldsymbol{\sigma} = \begin{Bmatrix} \sigma_{11} \\ \sigma_{22} \\ \sigma_{33} \\ \sigma_{12} \\ \sigma_{23} \\ \sigma_{31} \end{Bmatrix}, \quad \boldsymbol{\tau} = \begin{Bmatrix} \tau_{11} \\ \tau_{22} \\ \tau_{33} \\ \tau_{12} \\ \tau_{23} \\ \tau_{31} \end{Bmatrix}, \quad \boldsymbol{\varepsilon} = \begin{Bmatrix} \varepsilon_{11} \\ \varepsilon_{22} \\ \varepsilon_{33} \\ \varepsilon_{12} \\ \varepsilon_{23} \\ \varepsilon_{31} \end{Bmatrix}, \quad \mathbf{e} = \begin{Bmatrix} e_{11} \\ e_{22} \\ e_{33} \\ e_{12} \\ e_{23} \\ e_{31} \end{Bmatrix} \tag{40}$$

and

$$\frac{\partial \boldsymbol{\sigma}}{\partial \boldsymbol{\varepsilon}} = \begin{bmatrix} \frac{\partial \sigma_{11}}{\partial \varepsilon_{11}} & \frac{\partial \sigma_{11}}{\partial \varepsilon_{22}} & \frac{\partial \sigma_{11}}{\partial \varepsilon_{33}} & \frac{\partial \sigma_{11}}{\partial \varepsilon_{12}} & \frac{\partial \sigma_{11}}{\partial \varepsilon_{23}} & \frac{\partial \sigma_{11}}{\partial \varepsilon_{31}} \\ \frac{\partial \sigma_{22}}{\partial \varepsilon_{11}} & \frac{\partial \sigma_{22}}{\partial \varepsilon_{22}} & \frac{\partial \sigma_{22}}{\partial \varepsilon_{33}} & \frac{\partial \sigma_{22}}{\partial \varepsilon_{12}} & \frac{\partial \sigma_{22}}{\partial \varepsilon_{23}} & \frac{\partial \sigma_{22}}{\partial \varepsilon_{31}} \\ \frac{\partial \sigma_{33}}{\partial \varepsilon_{11}} & \frac{\partial \sigma_{33}}{\partial \varepsilon_{22}} & \frac{\partial \sigma_{33}}{\partial \varepsilon_{33}} & \frac{\partial \sigma_{33}}{\partial \varepsilon_{12}} & \frac{\partial \sigma_{33}}{\partial \varepsilon_{23}} & \frac{\partial \sigma_{33}}{\partial \varepsilon_{31}} \\ \frac{\partial \sigma_{12}}{\partial \varepsilon_{11}} & \frac{\partial \sigma_{12}}{\partial \varepsilon_{22}} & \frac{\partial \sigma_{12}}{\partial \varepsilon_{33}} & \frac{\partial \sigma_{12}}{\partial \varepsilon_{12}} & \frac{\partial \sigma_{12}}{\partial \varepsilon_{23}} & \frac{\partial \sigma_{12}}{\partial \varepsilon_{31}} \\ \frac{\partial \sigma_{23}}{\partial \varepsilon_{11}} & \frac{\partial \sigma_{23}}{\partial \varepsilon 22} & \frac{\partial \sigma_{23}}{\partial \varepsilon_{33}} & \frac{\partial \sigma_{23}}{\partial \varepsilon_{12}} & \frac{\partial \sigma_{23}}{\partial \varepsilon_{23}} & \frac{\partial \sigma_{23}}{\partial \varepsilon_{31}} \\ \frac{\partial \sigma_{31}}{\partial \varepsilon_{11}} & \frac{\partial \sigma_{31}}{\partial \varepsilon_{22}} & \frac{\partial \sigma_{31}}{\partial \varepsilon_{33}} & \frac{\partial \sigma_{31}}{\partial \varepsilon_{12}} & \frac{\partial \sigma_{31}}{\partial \varepsilon_{23}} & \frac{\partial \sigma_{31}}{\partial \varepsilon_{31}} \end{bmatrix} \tag{41}$$

It is worth mentioning that the above conversion of fourth/second order tensors to matrices/vectors was performed as described in [36]. The 2nd order Cauchy stress tensor is represented and implemented in OpenSees as a (6×1) vector, due to its symmetric property (i.e., $\sigma_{ij} = \sigma_{ji}$). The 4th order consistent tangent tensor, which is unsymmetrical (i.e., $C_{ijkl} \neq C_{klij}$) with minor-symmetry (i.e., $C_{ijkl} = C_{jikl} = C_{ijlk} = C_{jilk}$), is represented and implemented in OpenSees as a 6×6 matrix. However, the multiplication of two fourth/second order tensors cannot be directly converted to the multiplication of the corresponding matrices/vectors. For example, the constitutive law for linear elasticity, $\sigma_{ij} = C_{ijkl}\varepsilon_{kl}$, cannot be directly converted in matrix form as

$$\begin{Bmatrix} \sigma_{11} \\ \sigma_{22} \\ \sigma_{33} \\ \sigma_{12} \\ \sigma_{23} \\ \sigma_{31} \end{Bmatrix} \neq \begin{bmatrix} C_{11,11} & C_{11,22} & C_{11,33} & C_{11,12} & C_{11,23} & C_{11,31} \\ C_{22,11} & C_{22,22} & C_{22,33} & C_{22,12} & C_{22,23} & C_{22,31} \\ C_{33,11} & C_{33,22} & C_{33,33} & C_{33,12} & C_{33,23} & C_{33,31} \\ C_{12,11} & C_{12,22} & C_{12,33} & C_{12,12} & C_{12,23} & C_{12,31} \\ C_{23,11} & C_{23,22} & C_{23,33} & C_{23,12} & C_{23,23} & C_{23,31} \\ C_{31,11} & C_{31,22} & C_{31,33} & C_{31,12} & C_{31,23} & C_{31,31} \end{bmatrix} \times \begin{Bmatrix} \varepsilon_{11} \\ \varepsilon_{22} \\ \varepsilon_{33} \\ \varepsilon_{12} \\ \varepsilon_{23} \\ \varepsilon_{31} \end{Bmatrix} \tag{42}$$

Instead, it should be converted to

$$\begin{Bmatrix} \sigma_{11} \\ \sigma_{22} \\ \sigma_{33} \\ \sigma_{12} \\ \sigma_{23} \\ \sigma_{31} \end{Bmatrix} = \begin{bmatrix} C_{11,11} & C_{11,22} & C_{11,33} & 2C_{11,12} & 2C_{11,23} & 2C_{11,31} \\ C_{22,11} & C_{22,22} & C_{22,33} & 2C_{22,12} & 2C_{22,23} & 2C_{22,31} \\ C_{33,11} & C_{33,22} & C_{33,33} & 2C_{33,12} & 2C_{33,23} & 2C_{33,31} \\ C_{12,11} & C_{12,22} & C_{12,33} & 2C_{12,12} & 2C_{12,23} & 2C_{12,31} \\ C_{23,11} & C_{23,22} & C_{23,33} & 2C_{23,12} & 2C_{23,23} & 2C_{23,31} \\ C_{31,11} & C_{31,22} & C_{31,33} & 2C_{31,12} & 2C_{31,23} & 2C_{31,31} \end{bmatrix} \times \begin{Bmatrix} \varepsilon_{11} \\ \varepsilon_{22} \\ \varepsilon_{33} \\ \varepsilon_{12} \\ \varepsilon_{23} \\ \varepsilon_{31} \end{Bmatrix} \tag{43}$$

Thus, special functions need to be programmed for the tensor multiplication purposes.

5 Application examples

5.1 Three-dimensional solid block subjected to quasi-static cyclic loading

The first application example considered was developed for the purpose of verifying and validating the newly developed algorithm to compute the consistent tangent moduli for the multi-yield-surface J_2 plasticity model in the context of a very simple academic example exhibiting 3D stress–strain response. Thus, a three-dimensional (3D) solid block of dimensions 1 m × 1 m × 1 m subjected to quasi-static cyclic loading in both horizontal directions simultaneously, see Fig. 5, is used as first application and validation example. The block is discretized into 8 brick elements defined as displacement-based eight-noded, trilinear isoparametric finite elements with eight integration points each. The material properties of the block are taken as similar to those of an undrained medium clay [13], i.e., low-strain shear modulus $G = 6.0 \times 10^4$ kPa, elastic bulk modulus $B = 2.4 \times 10^5$ kPa, and maximum shear stress $\tau_{max} = 30$ kPa. The points (τ_j, γ_j) defining the piecewise linear approximation of the $\tau - \gamma$ backbone curve are defined such that their projections on the τ axis are uniformly spaced (see Fig. 1). The bottom nodes of the finite element (FE) model are fixed and top nodes {A, B, C} and {A, D, E} are subjected to harmonic 90 degrees out-of-phase concentrated horizontal forces $F_{x_1}(t) = 2.0\sin(0.2\pi t)$ kN and $F_{x_2}(t) = 2.0\sin(0.2\pi t + 0.5\pi)$ kN, respectively, as shown in Fig. 5. The number of yield surfaces is set to 20 unless specified otherwise. A time increment of $\Delta t = 1.00$ s is used to integrate the quasi-static equations of equilibrium.

The force $F_{x1}(t)$-displacement (at node A in the X_1-direction) response is shown in Fig. 6, while the hysteretic

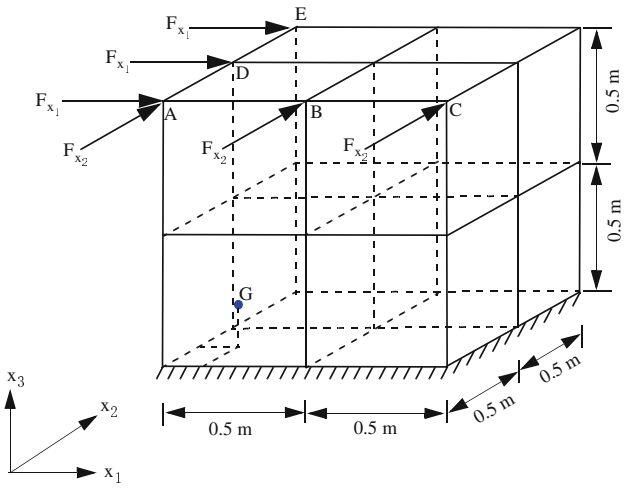

Fig. 5 Solid block of clay subjected to horizontal quasi-static cyclic loading

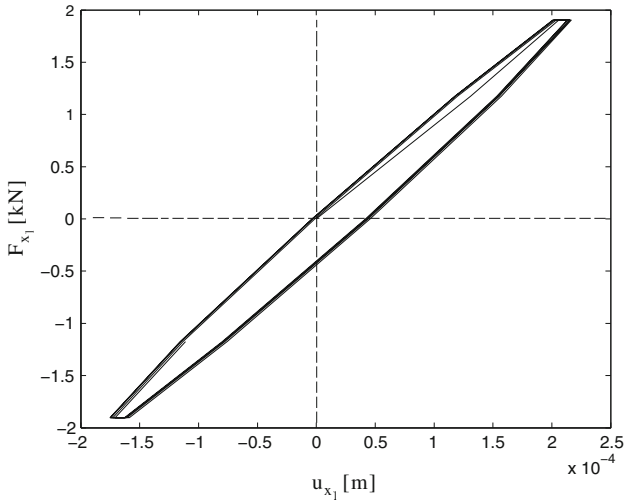

Fig. 6 Force–displacement response at node A

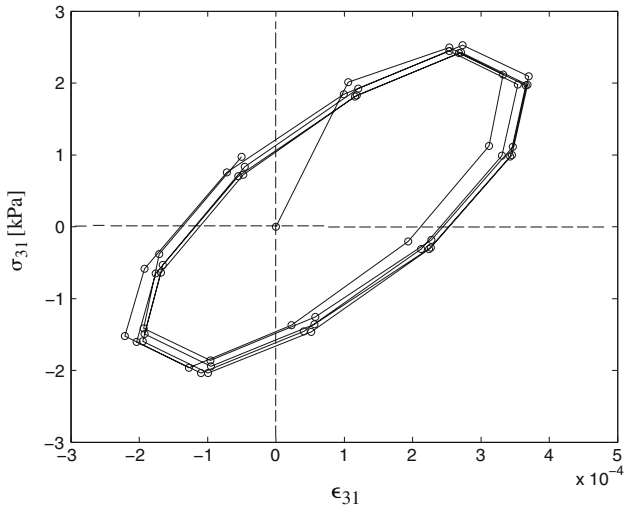

Fig. 7 Shear stress–strain response at Gauss point G (see Fig. 5)

shear stress–strain response $\sigma_{31} - \varepsilon_{31}$ at Gauss point G (see Fig. 5) is plotted in Fig. 7. This last figure shows that the clay material undergoes significant yielding under the cyclic loading considered.

5.1.1 *Comparison of convergence rate and computational time between the use of consistent and continuum tangent moduli*

This section examines the rate of convergence of the Newton–Raphson iterations at the "structure" level obtained when using the material consistent versus continuum tangent moduli in solving the problem presented in Fig. 5. A tolerance of 10^{-4} kN on the norm of the unbalanced force vector is used as convergence criterion in the analyses presented in this section. The comparison result is shown in Fig. 8, and the computational time is provided in the legend. The computational time (clock time and not CPU time) depends on the CPU speed, memory capability, and background processes in the computer. Since for each comparison, the two problems are run sequentially on the same computer, the computational time can be used to compare the speeds of the two Newton–Raphson iterative algorithms. Figure 9 shows the norm of the unbalanced force vector as a function of the iteration number for a representative load step (step # 20) computed using the material continuum and consistent tangent moduli, respectively.

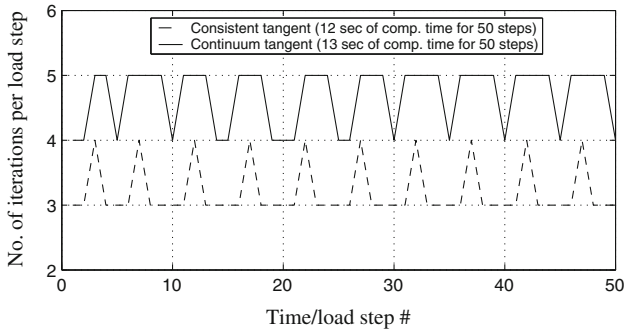

Fig. 8 Convergence rate comparison (convergence test based on norm of unbalanced force vector with tol $= 10^{-4}$ kN)

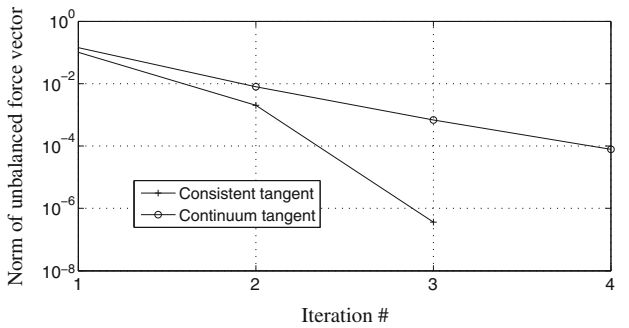

Fig. 9 Norm of unbalanced force vector versus iteration number in load step # 20 (tol $= 10^{-4}$ kN)

From the results obtained for this benchmark problem, the following observations can be made:

- From Fig. 9, it is observed that when using the material consistent tangent moduli, the norm of the unbalanced force vector follows an asymptotic rate of quadratic convergence as expected [2], which is not the case when using the continuum tangent moduli.
- The number of iterations per load step is consistently lower (by 20–40%) when using the consistent instead of the continuum tangent moduli.
- The use of either the consistent or continuum tangent moduli leads to about the same computational time. This is due to the fact that although the use of the consistent tangent moduli reduces the number of Newton–Raphson

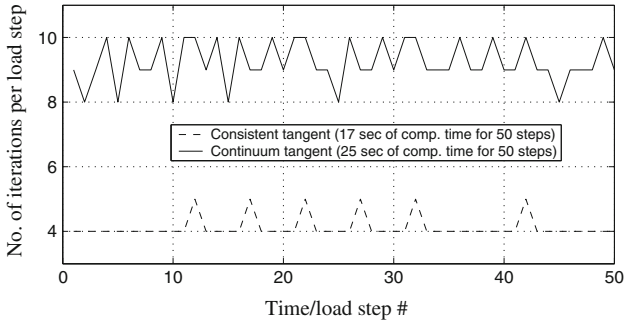

Fig. 10 Convergence rate comparison (convergence test based on norm of unbalanced force vector with tol $= 10^{-8}$ kN)

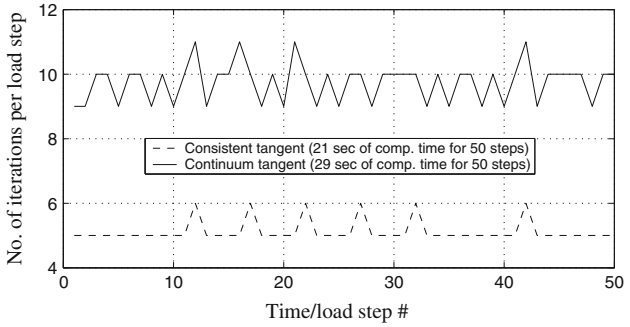

Fig. 11 Convergence rate comparison (convergence test based on norm of incremental displacement vector with tol $= 10^{-12}$ m)

iterations, it requires more computations to form the tangent stiffness matrix.

5.1.2 *Comparison of convergence rate for smaller convergence tolerance*

In this section, the above benchmark problem is solved with tighter convergence tolerances. The computational conditions are the same, except for the convergence tolerances that are set to 10^{-8} kN, 10^{-12} m, and 10^{-20} kN m for the convergence criteria based on the norm of the unbalanced force vector, the norm of the incremental displacement vector, and the energy increment, respectively. The number of Newton–Raphson iterations needed to reach convergence at each time or load step when using the material continuum and material consistent tangent moduli are compared in Figs. 10, 11 and 12. At representative load step # 15, the norm of the unbalanced force vector, the norm of the incremental displacement vector and the energy increment as a function of the iteration number are shown in Figs. 13, 14 and 15, respectively, when using both the continuum and consistent tangent material moduli. These results show that the convergence rate is significantly higher and the computational time significantly lower when using the consistent over the continuum tangent moduli. The asymptotic rate of quadratic convergence is again clearly observed in Fig. 13.

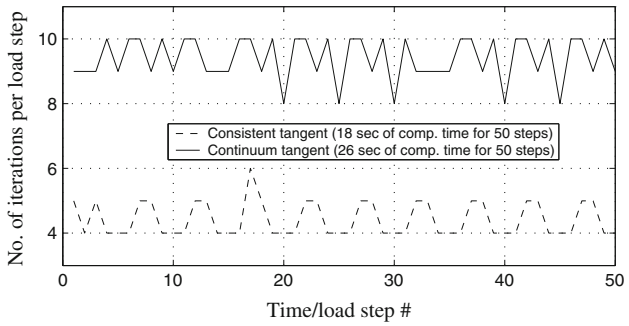

Fig. 12 Convergence rate comparison (convergence test based on energy increment with tol $= 10^{-20}$ kN m)

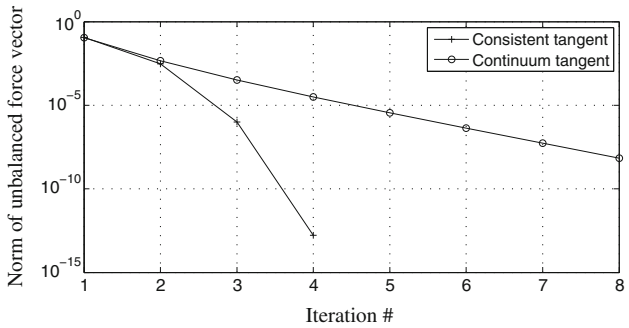

Fig. 13 Norm of unbalanced force vector versus iteration number in load step # 15 (tol $= 10^{-8}$ kN)

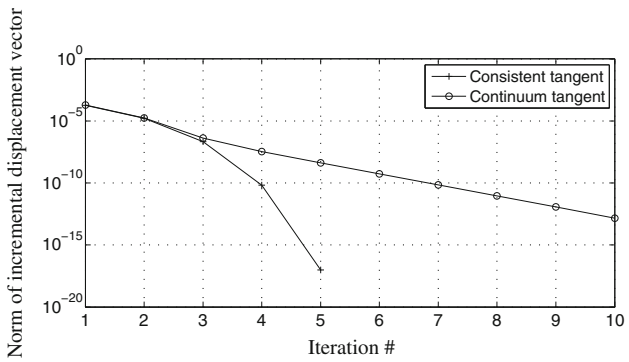

Fig. 14 Norm of incremental displacement vector versus iteration number in load step # 15 (tol $= 10^{-12}$ m)

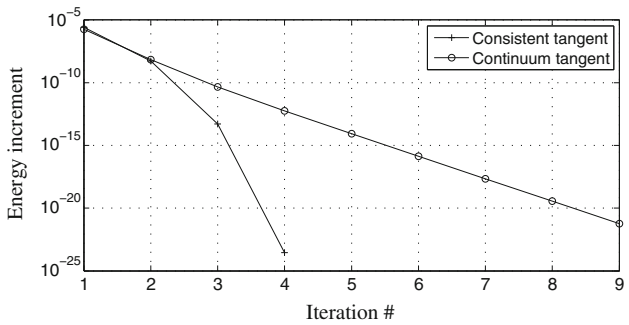

Fig. 15 Energy increment versus iteration number in load step # 15 (tol $= 10^{-20}$ kN m)

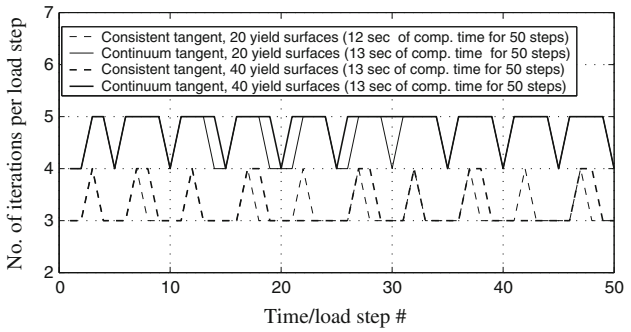

Fig. 16 Convergence rate comparison for varying number of yield surfaces (convergence test based on norm of unbalanced force vector with tol $= 10^{-4}$ kN)

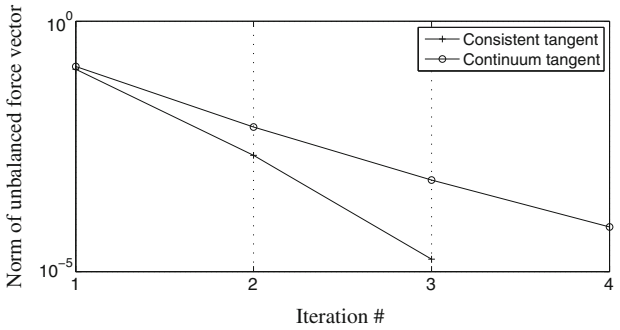

Fig. 17 Norm of unbalanced force vector versus iteration number in load step # 10 (tol $= 10^{-4}$ kN, 40 yield surfaces)

By comparing the results in Sects. 5.1.1 and 5.1.2, it is observed that the advantage of using the consistent over the continuum tangent moduli becomes more pronounced (in terms of both the number of N-R iterations per step and the total computational time) with decreasing convergence tolerance. Only when the tolerance is small enough such that the sequence of trial stresses $\boldsymbol{\tau}_i^{\text{tr}}$ (see Fig. 2) approaches the solution point from within the convergence region, does the use of the consistent tangent moduli reach a quadratic rate of convergence of the Newton–Raphson iterative process.

5.1.3 Convergence rate comparison for varying number of yield surfaces

This section examines the effect of using 40 versus 20 yield surfaces in defining the backbone curve of the material constitutive model, on the convergence rate of the Newton–Raphson iterative process. The comparative results are shown in Figs. 16 and 17. The convergence criterion used to perform the simulation for 40 yield surfaces is the same as those in Sect. 5.1.1 (for 20 yield surfaces), i.e., tolerance = 10^{-4} kN for norm of unbalanced force vector. These comparative results show that the convergence rate is faster when using the consistent over the continuum tangent moduli, regardless of the number of yield surfaces used in the material constitutive model. In this comparative example, the difference in the convergence rate obtained by using the consistent versus continuum tangent moduli is not significant due to the relaxed convergence tolerance used in the computations. It is interesting to note that at this time step, the quadratic convergence rate is not observed in Fig. 17. This is due to the fact that when the convergence tolerance is too large, the quadratic convergence rate corresponding to the use of the consistent tangent moduli is not reached before convergence is achieved.

Table 1 Material properties of various layers of soil column (from top to bottom)

Material #	G (KPa)	$\tau_{\max}$ (KPa)
1	54,450	33
2	33,800	26
3	96,800	44
4	61,250	35
5	180,000	60
6	369,800	86

5.2 Multi-layered soil column subjected to earthquake base excitation

The second benchmark problem consists of a multi-layered soil column subjected to earthquake base excitation. This soil column is representative of the local soil condition at the site of the Humboldt Bay Middle Channel Bridge near Eureka in Northern California [13]. A Multi-yield-surface J_2 plasticity model with 20 yield surfaces and different parameter sets given in Table 1 is used to represent the various soil layers. The soil column is discretized into a 2D plane-strain finite element model consisting of 28 four-node quadratic bilinear isoparametric elements with 4 Gauss points each as shown in Fig. 18. The soil column is assumed to be under simple shear condition, and the corresponding nodes at the same depth on the left and right boundaries are tied together for both horizontal and vertical displacements. The presented method of modeling the simple shear condition for a 2D soil domain is commonly used in geotechnical earthquake engineering [11,33,37]. There are two sources of energy dissipation used in this soil column model: (1) the hysteretic energy dissipation through inelastic action of the soil material (as modeled explicitly using the multi-yield surface J_2 plasticity model), and (2) some numerical/algorithmic damping due to the fact that $\gamma > 0.5$ in the Newmark-beta time integration method used, with parameters $\beta = 0.275625$, $\gamma = 0.55$ and a constant time step $\Delta t = 0.01$ s, for integrating the equations of motion of the system. The total horizontal acceleration at the base of the soil column, see Fig. 19, was obtained

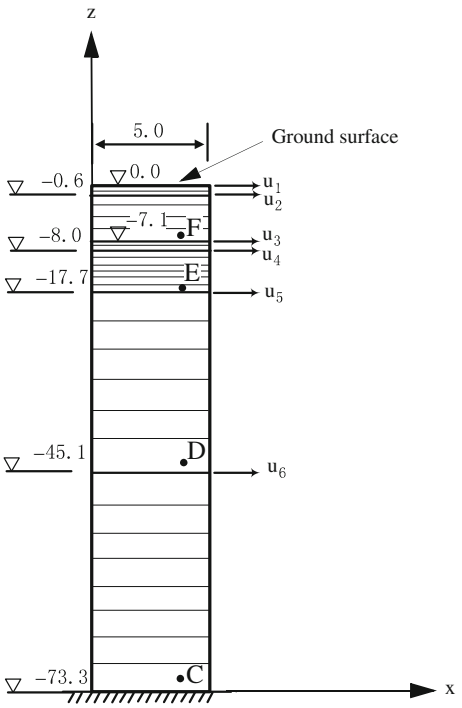

Fig. 18 Layered soil column subjected to total base acceleration with finite element mesh shown in thin line (unit: m)

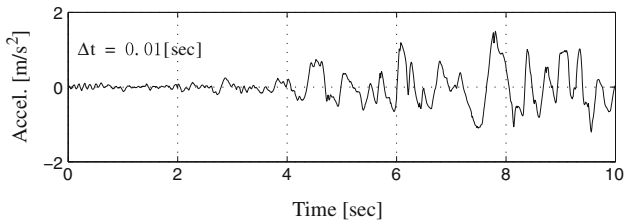

Fig. 19 Total acceleration at the base of the soil column

elsewhere [13] through deconvolution of a ground surface free field motion. The horizontal displacement response of the soil column (relative to the base) at the top of each soil layer is shown in Fig. 20. The shear stress–strain (σ_{xz}, ε_{xz}) responses at Gauss points C, D, E, F (see Fig. 18) of the soil column are shown in Fig. 21. The response simulation results in Figs. 20 and 21 indicate that the soil materials undergo significant nonlinear behavior during the earthquake.

5.2.1 *Comparison of convergence rate and computational time between the use of consistent and continuum tangent moduli*

In this section, the number of iterations to reach convergence at every time step is investigated when using the material consistent versus continuum tangent moduli. Comparative results are given in Fig. 22 where the convergence criterion is based on the norm of the unbalanced force vector

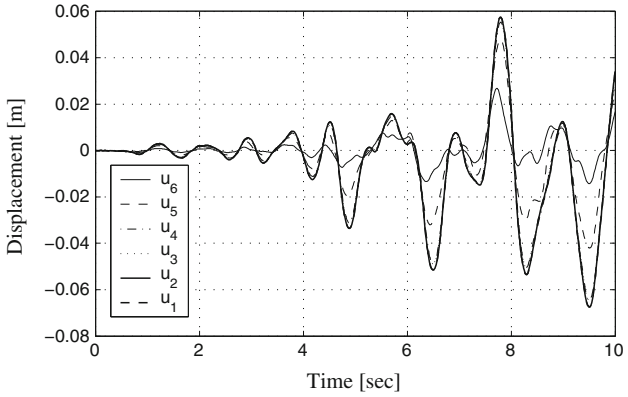

Fig. 20 Relative horizontal displacement response histories at the top of each layer of the soil column (see Fig. 18)

(tolerance = 10^{-4} kN). At the representative time step # 800, the norm of the unbalanced force vector is shown as a function of the iteration number in Fig. 23, for both cases of using the consistent and continuum tangent moduli.

From these results, the following observations can be made:

- From Fig. 23, it is observed that the asymptotic rate of quadratic convergence of the norm of the unbalanced force vector guaranteed by Newton–Raphson method when using the consistent tangent moduli is more than achieved.
- The number of iterations per time step is typically lower (by 0–40%) when using the consistent over the continuum tangent moduli.
- Using the consistent tangent moduli saves computational time by about 15%.

5.2.2 *Comparison of convergence rate for smaller convergence tolerance*

In this section, the dynamic response analysis presented above is reconsidered with a tighter (smaller) convergence tolerance. The computational conditions remain the same, except for the convergence tolerances which are set to: 10^{-8} kN, 10^{-12} m, and 10^{-20} kN m for the convergence criteria based on the norm of the unbalanced force vector, the norm of the incremental displacement vector, and the energy increment, respectively. Results on the number of iterations required for each time step are given in Figs. 24, 25 and 26. For the representative time step # 700, the norm of the unbalanced force vector, the norm of the last incremental displacement vector and the energy increment are plotted in Figs. 27, 28 and 29, respectively, as a function of the iteration number.

These results demonstrate that the use of the material consistent tangent moduli reduces the number of iterations needed to achieve convergence by 20–45% and the

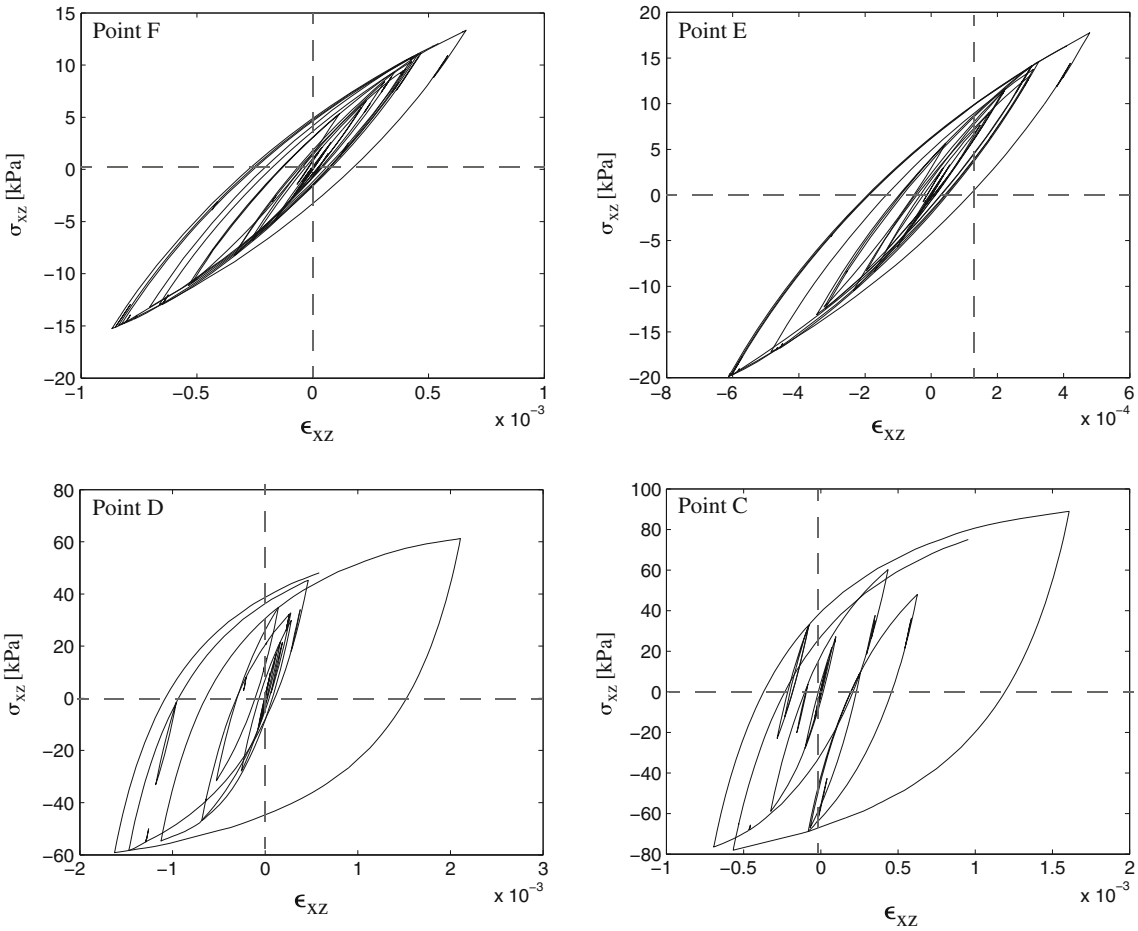

Fig. 21 Shear stress–strain hysteretic response at Gauss points C, D, E, and F (see Fig. 18)

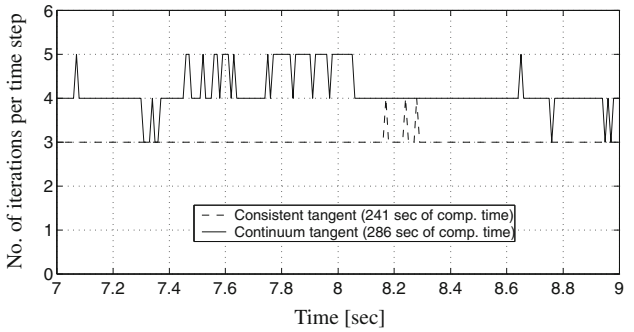

Fig. 22 Convergence rate comparison (convergence test based on norm of unbalanced force vector with tol $= 10^{-4}$ kN)

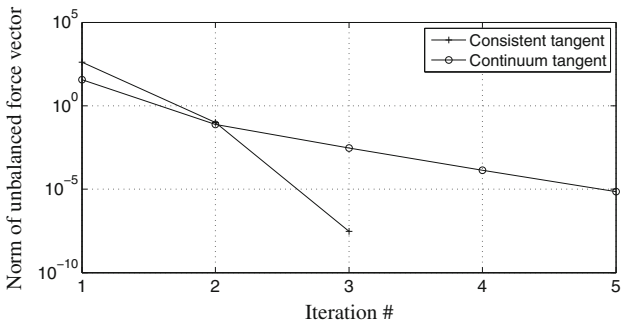

Fig. 23 Norm of unbalanced force vector versus iteration number at time step # 800 (tol $= 10^{-4}$ kN m)

computational time by 10–40%, when compared with the use of the continuum tangent moduli. By comparing results in Sects. 5.2.1 and 5.2.2, it is observed as in the previous benchmark problem that the advantage of using the consistent tangent moduli over the continuum tangent moduli is more pronounced as the convergence tolerance becomes tighter (smaller).

5.2.3 Comparison of convergence rate for varying time step size

In this section, the convergence rate and computational time are compared between the use of the consistent and continuum tangent moduli when the time step is purposely exaggeratedly increased to $\Delta t = 0.05$ s, with all other conditions remaining the same as in Sect. 5.2.1. The comparative results

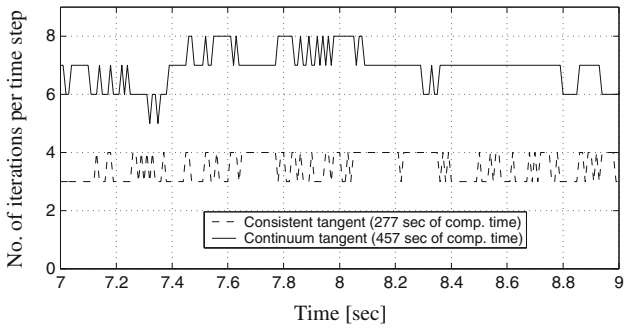

Fig. 24 Convergence rate comparison (convergence test based on norm of unbalanced force vector with tol $= 10^{-8}$ kN)

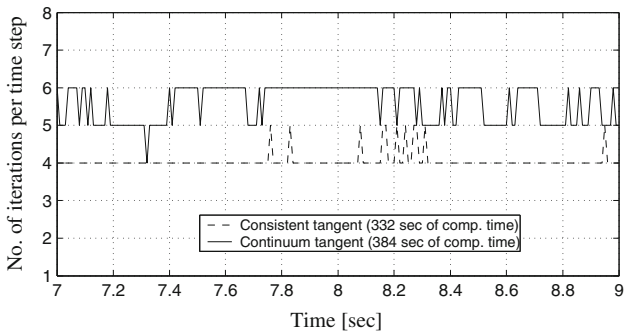

Fig. 25 Convergence rate comparison (convergence test based on norm of incremental displacement vector with tol $= 10^{-12}$ m)

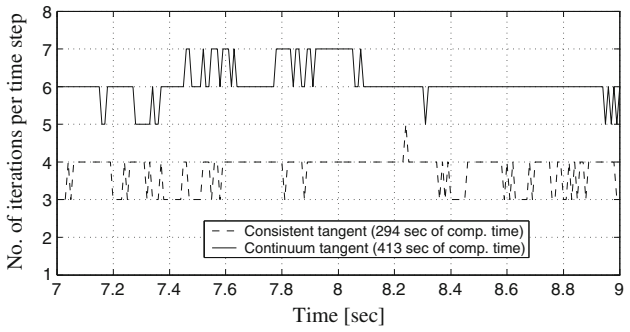

Fig. 26 Convergence rate comparison (convergence test based on energy increment with tol $= 10^{-20}$ kN m)

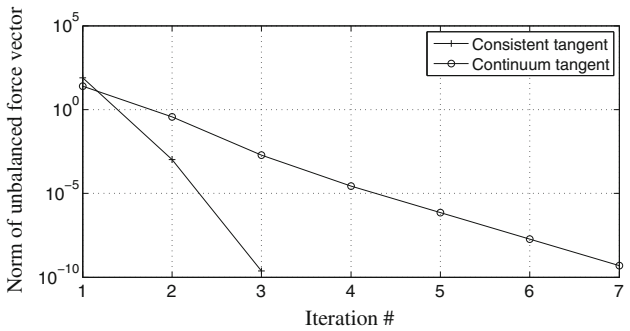

Fig. 27 Norm of unbalanced force vector versus iteration number at time step # 700 (tol $= 10^{-8}$ kN)

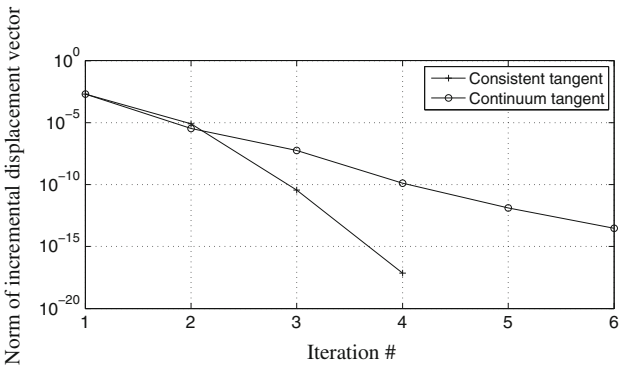

Fig. 28 Norm of incremental displacement vector versus iteration number at time step # 700 (tol $= 10^{-12}$ m)

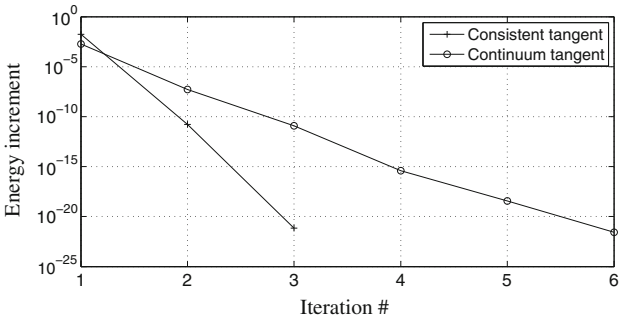

Fig. 29 Energy increment versus iteration number at time step # 700 (tol $= 10^{-20}$ kN m)

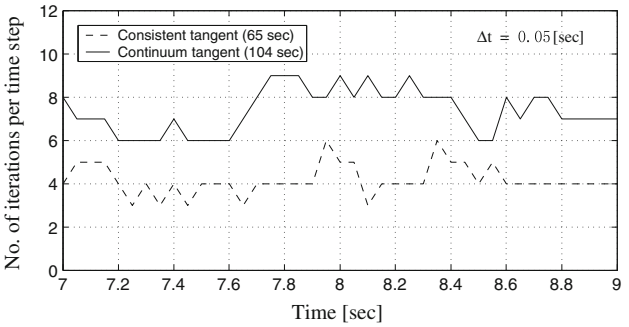

Fig. 30 Convergence rate comparison (convergence test based on norm of unbalanced force vector with tol $= 10^{-4}$ kN, $\Delta t = 0.05$ s)

are plotted in Figs. 30, 31 and 32. For the representative time step # 160 ($t = 8.00$ s), the norm of the unbalanced force vector, the norm of the incremental displacement vector and the energy increment are shown in Figs. 33, 34 and 35, respectively, for both cases of using the consistent and continuum tangent moduli.

From these results, it is observed that in this case the use of the consistent tangent moduli reduces the number of iterations per time step needed to achieve convergence by 18–40%, and the computational time by 10–38%. Comparing the results in Sect. 5.2.3 with their counterparts in Sect. 5.2.1, it is observed that when the time step is increased,

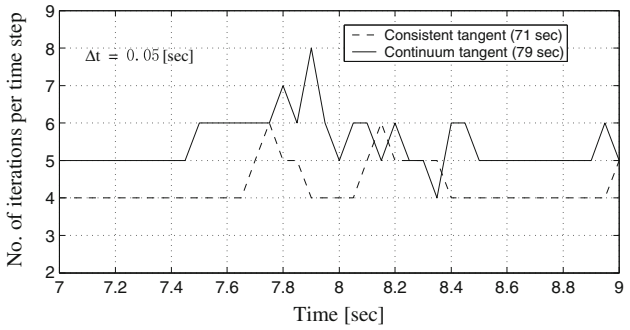

Fig. 31 Convergence rate comparison (convergence test based on norm of incremental displacement vector with tol $= 10^{-8}$ m, $\Delta t = 0.05$ s)

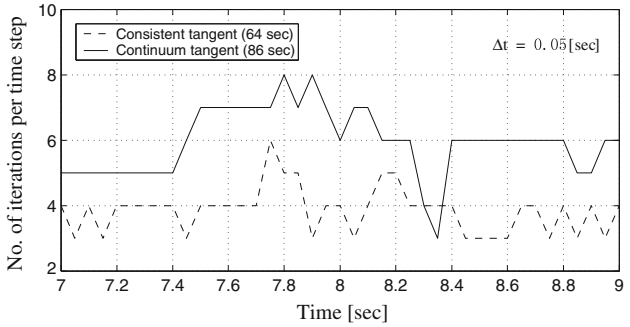

Fig. 32 Convergence rate comparison (convergence test based on energy increment with tol $= 10^{-12}$, $\Delta t = 0.05$ s)

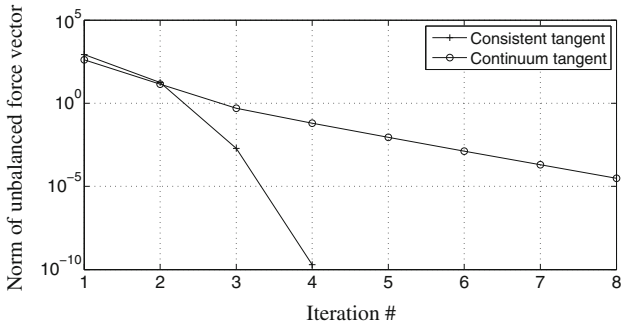

Fig. 33 Norm of unbalanced force vector versus iteration number at time step # 160 (tol $= 10^{-4}$ kN, $\Delta t = 0.05$ s)

the advantage of using the consistent over the continuum tangent moduli becomes more pronounced. When the time step size increases, the difference between the constitutive equations $\Delta\boldsymbol{\sigma} = \Delta\boldsymbol{\sigma}(\Delta\boldsymbol{\varepsilon})$ and $\dot{\boldsymbol{\sigma}} = \dot{\boldsymbol{\sigma}}(\dot{\boldsymbol{\varepsilon}})$ becomes more significant, as does the difference between the differentiations $\mathrm{d}(\Delta\boldsymbol{\sigma}) = \mathrm{d}(\Delta\boldsymbol{\varepsilon})$ and $\dot{\boldsymbol{\sigma}}/\dot{\boldsymbol{\varepsilon}} = \mathrm{d}\boldsymbol{\sigma}/\mathrm{d}\boldsymbol{\varepsilon}$, which are defined as consistent tangent moduli and continuum tangent moduli, respectively. As the time step size increases, the continuum tangent moduli become more 'inconsistent' with the Newton process, thus leading to the loss of the asymptotic rate of quadratic convergence characteristic of Newton's method.

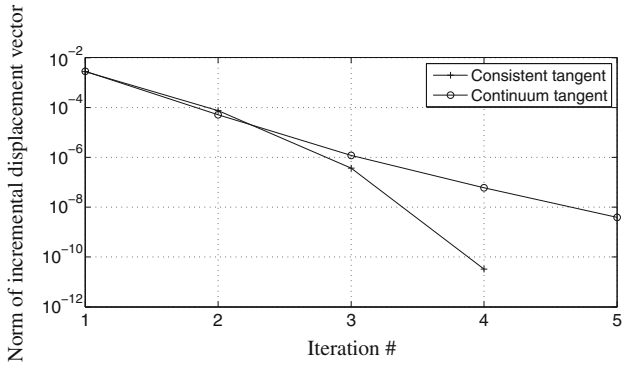

Fig. 34 Norm of incremental displacement vector versus iteration number at time step # 160 (tol $= 10^{-8}$ m, $\Delta t = 0.05$ s)

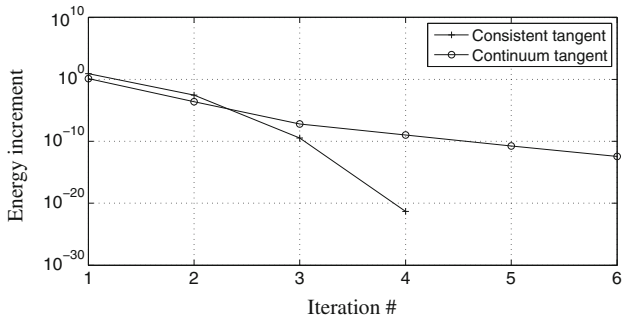

Fig. 35 Energy increment versus iteration number at time step # 160 (tol $= 10^{-12}$ kN m, $\Delta t = 0.05$ s)

5.2.4 *Convergence rate comparison for varying number of yield surfaces*

This section examines the effect on the convergence rate of using 40 versus 20 yield surfaces in the constitutive models of the various soil layers with all other modeling assumptions and computational conditions (including the convergence criterion and tolerance) remaining the same as in Sect. 5.2.1. The comparative results are shown in Figs. 36 and 37. Comparing the results in Sect. 5.2.4 with those in Sect. 5.2.1, it is noticed that the convergence rate is faster when using the consistent over the continuum tangent moduli, regardless of the number of yield surfaces used in the soil material models.

5.3 Three-dimensional pile–soil interaction system subjected to quasi-static cyclic loading

The last application example consists of a cylindrical concrete pile of 0.75 m diameter embedded in a layered clay soil (see Fig. 38). The segment of the pile above ground is 6 m long and discretized into 4 beam-column elements, while the embedded portion of the pile is 6 m long and discretized into 5 beam-column elements. The pile is assumed to be linear elastic with the following cross-section properties: Young's modulus E = 3.00E7 kPa, Area A = 0.44 m^2, Moment of

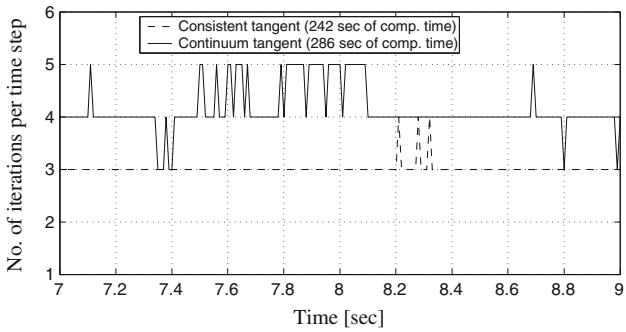

Fig. 36 Convergence rate comparison (convergence test based on norm of unbalanced force vector with tol $= 10^{-4}$ kN, 40 yield surfaces)

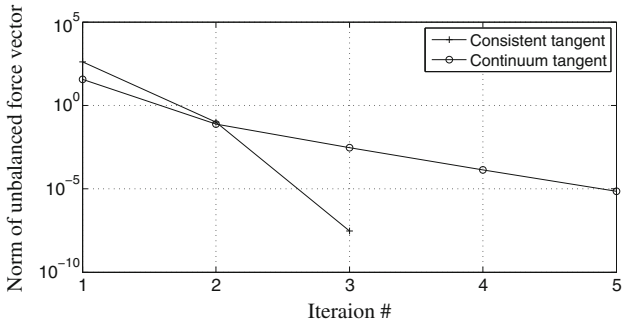

Fig. 37 Norm of unbalanced force vector versus iteration number at time step # 800 (tol $= 10^{-4}$ kN, 40 yield surfaces)

inertia I $= 4.90\text{E}{-2}\,\text{m}^4$. The foundation soil is stratified into four distinct layers of clay materials of thicknesses 2, 3, 3, and 2 m, respectively, from top to bottom. A computational soil domain of size 28.8 m (length) by 28.8 m soil (width) by 10 m (depth) is discretized into 576 8-node (displacement-based) brick elements as shown in Fig. 38. The FE mesh was created using a finite element user-interface for 3D analysis of lateral pile–ground interaction system response, OpenSeesPL [38]. The soil material in each layer is modeled using a 20-yield-surfaces multi-yield-surface J_2 plasticity model with material parameters varying across layers. The soil properties are the same as those of the top four layers of soil in the second application example described in Sect. 5.2; these properties are given in Table 1 (Material # 1 through 4), and a Poisson's ratio of 0.35 was used for all soil materials.

Below ground, sets of 16 radial rigid beam-column links, normal to the pile longitudinal axis, are used to represent the geometric space occupied by the pile. The soil 3D brick element nodes at the periphery of the pile are connected to the pile geometric configuration at the corresponding outer nodes of these rigid links using the equalDOF constraint in OpenSees for translations only as shown in Fig. 38 [23].

A simple shear condition is used by constraining the longitudinal/transversal mesh lateral boundaries to undergo the same vertical and longitudinal/transversal motions, using the equalDOF constraint in OpenSees. To exercise the 3D response behavior of the foundation soil as would be the case for a pile foundation supporting a column of a bridge subjected to bi-directional horizontal earthquake excitation, the top of the pile is subjected quasi-statically to two harmonic 90 degrees out-of-phase concentrated horizontal (lateral) forces $\text{F}_\text{x}(t) = 2.0\sin(0.2\pi t)$ kN and $\text{F}_\text{y}(t) = 2.0\sin(0.2\pi t + 0.5\pi)$ kN, respectively. This loading condition corresponds to a radial lateral 120 kN force rotating at the angular velocity of 0.1 cycle per second. The duration of the loading is 10 s, which corresponds to one cycle of harmonic loading. To avoid convergence problems in integrating the quasi-static nonlinear equations of equilibrium, an adaptive

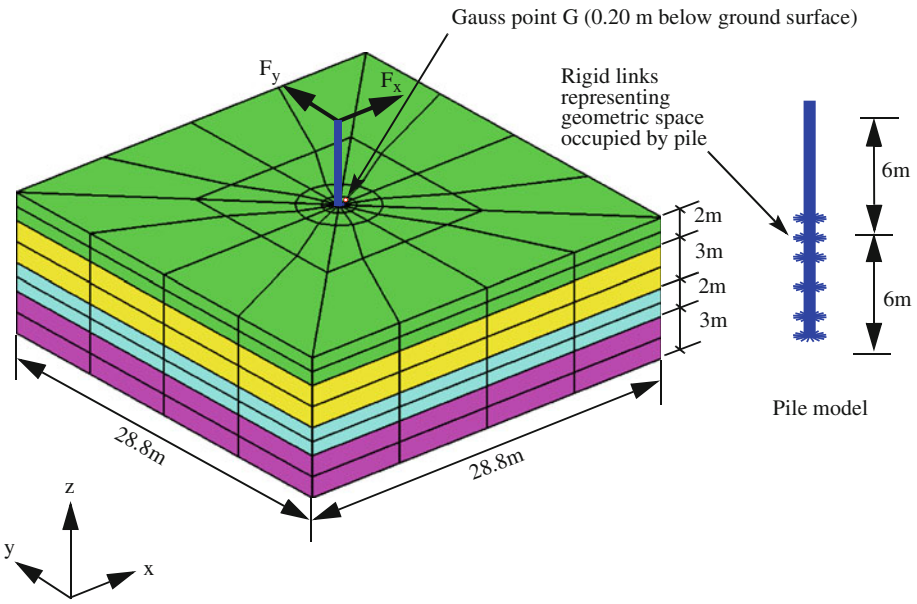

Fig. 38 Three-dimensional pile–soil interaction system subjected to quasi-static cyclic loading

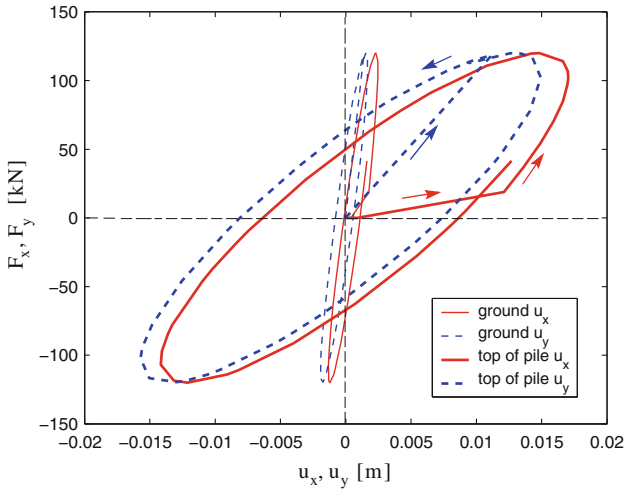

Fig. 39 Force–displacement response of top of pile

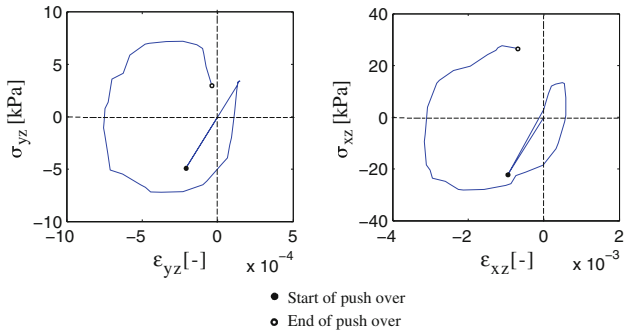

Fig. 40 Shear stress–strain responses at Gauss point G (see Fig. 38)

time/load stepping scheme is used with $\Delta t_{\max} = 0.5$ s and $\Delta t_{\min} = 0.01$ s.

The horizontal force-displacement response histories, $F_x - u_x$ and $F_y - u_y$, at the top of the pile and at the center of the pile at the ground surface level are shown in Fig. 39, while the hysteretic shear stress–strain responses, $\sigma_{yz} - \varepsilon_{yz}$ and $\sigma_{xz} - \varepsilon_{xz}$, at Gauss point G (located 0.53 m from the center of the pile and 0.20 m under the ground surface, see Fig. 38) are plotted in Fig. 40. A maximum shear stress ratio of 0.92 was developed at this Gauss point during the quasi-static push-over. Here, the shear stress ratio is defined as the octahedral shear stress demand over the shear strength. This last figure shows that the clay material near the pile and near the ground surface undergoes significant yielding under the cyclic loading considered.

5.3.1 *Comparison of convergence rate and computational time between the use of consistent and continuum tangent moduli*

This section examines the rate of convergence of the Newton–Raphson iterative process at the "structure" level

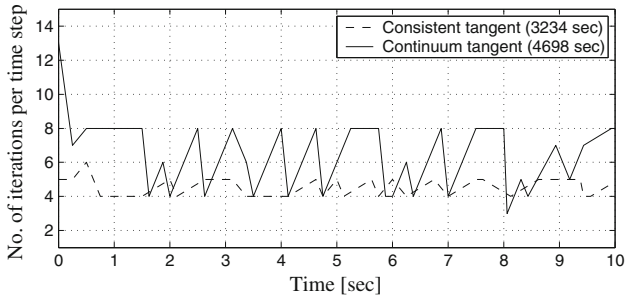

Fig. 41 Convergence rate comparison (convergence test based on norm of unbalanced force vector with tol $= 10^{-3}$ kN)

obtained when using the material consistent versus continuum tangent moduli in solving the present pile–soil interaction problem. A tolerance of 10^{-3} kN on the norm of the unbalanced force vector is used as convergence criterion in the analyses presented in this section. The comparison results are shown in Fig. 41. Table 2 provides, at a number of representative load steps, the norm of the unbalanced force vector as a function of the iteration number obtained when using the material consistent versus continuum tangent moduli. From the results obtained for this benchmark problem, it is observed that:

- From Table 2, it is observed that when using the material consistent tangent moduli, the norm of the unbalanced force vector exhibits the asymptotic rate of quadratic convergence as expected, which is not the case when using the continuum tangent moduli. It is noteworthy that at time step $t = 5$ s, the convergence rate achieved using consistent tangent moduli has not reached yet the quadratic rate at the last (converged) iteration (i.e., the unbalanced force norm is 4.46×10^{-3} at the 4th iteration, and only 3.38×10^{-5} at the 5th iteration). This is due to the fact that the limit of the computational accuracy has been reached for this problem, which was found (by trial-and-error) to be 5.0×10^{-5} for the norm of the unbalanced force vector. This limit is due to various sources of numerical noise in the algorithms involved including round-off errors.
- The number of iterations per load step required to reach convergence is consistently lower when using the consistent over the continuum tangent moduli. The average number of iterations per load step needed when using the consistent and continuum tangent moduli is 4.5 and 6.3, respectively (i.e., use of the consistent tangent moduli reduces the average number of iterations per time/load step by 29% in this case).
- The use of the consistent over continuum tangent moduli reduces the computational time by 31% in this case.

Table 2 Norm of unbalanced force vector versus iteration number (tol $= 10^{-3}$ kN)

Pseudo time (s)	Iteration #	1	2	3	4	5	6	7	8
1.0	Consistent tangent	5.92	8.14E−1	2.87E−2	3.53E−5				
1.0	Continuum tangent	7.49	1.45	2.67E−1	6.27E−2	1.60E−2	5.40E−3	3.84E−3	2.76E−4
3.125	Consistent tangent	1.42E1	2.17	2.16E−1	1.37E−2	2.61E−5			
3.125	Continuum tangent	7.12	1.48	3.69E−1	9.63E−2	2.58E−2	7.26E−3	2.13E−3	6.52E−4
5.0	Consistent tangent	7.35	9.86E−1	2.97E−2	4.46E−3	3.38E−5			
5.25	Continuum tangent	7.07	1.49	3.87E−1	9.67E−2	2.45E−2	6.57E−3	1.82E−3	5.19E−4
7.0	Consistent tangent	6.56	9.22E−1	3.91E−2	3.72E−4				
7.0	Continuum tangent	1.35	7.33E−2	5.57E−3	5.04E−4				
9.125	Consistent tangent	1.29E1	1.99	5.31E−1	1.01E−2	4.68E−5			
8.9375	Continuum tangent	6.70	1.27	3.63E−1	1.08E−1	1.65E−2	3.66E−3	9.58E−4	

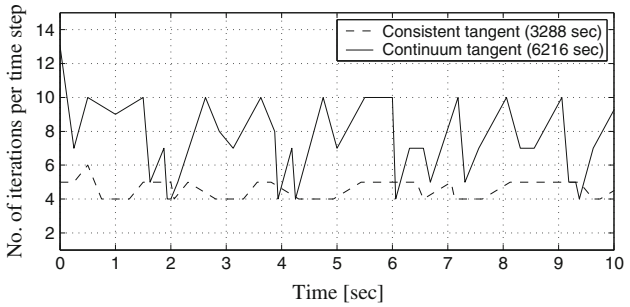

Fig. 42 Convergence rate comparison (convergence test based on norm of unbalanced force vector with tol $= 10^{-4}$ kN)

5.3.2 Comparison of convergence rate for smaller convergence tolerance

In this section, the above considered benchmark problem is solved using a tighter convergence tolerance. The tolerance on the norm of the unbalanced force vector is reduced from 1×10^{-3} to 1×10^{-4} kN. The number of Newton–Raphson iterations needed to reach convergence at each time/load step when using the consistent and continuum tangent moduli are compared in Fig. 42. The norm of the unbalanced force vector versus iteration number when using the consistent and continuum tangent moduli is reported in Table 3 for several representative time/load steps. These results show that the convergence rate is significantly higher (with average number of iterations per load step reduced by 38%) and the computational time significantly lower (by 47%) when using the consistent over the continuum tangent moduli. The asymptotic rate of quadratic convergence obtained when using the consistent tangent moduli is again clearly observed in Table 3. It is also observed from this table that the norm of the unbalanced force vector cannot be reduced below 1×10^{-5} due to various sources of numerical noise in the various algorithms involved including round-off errors. Furthermore, when the convergence tolerance for the norm of the unbalanced force vector is set to 5×10^{-5}, the Newton iteration process using the consistent tangent moduli converges almost at the same rate as that shown in Fig. 42, while it does not converge to the required tolerance when using the continuum tangent moduli. Thus, in this case, the use of the consistent tangent moduli enables convergence of the Newton process, which cannot be achieved using the continuum tangent moduli.

By comparing the results in Sects. 5.3.1 and 5.3.2, it is observed as in the previous examples that the advantage of using the consistent over the continuum tangent moduli becomes more pronounced (in terms of both the number of N-R iterations per step and the total computational time) with decreasing convergence tolerance.

Table 3 Norm of unbalanced force vector versus iteration number (tol $= 10^{-4}$ kN)

Pseudo time (s)	Iteration #	1	2	3	4	5	6	7	8	9	10
1.0	Consistent tangent	5.92	8.14E−1	2.87E−2	3.53E−5						
1.0	Continuum tangent	7.26	1.43	2.63E−1	6.12E−2	1.53E−2	5.22 E−3	3.82 E−3	2.41E−4	6.89E−5	
2.8125	Consistent tangent	14.4	2.16	1.87E−1	5.32E−5						
3.125	Continunm tangent	2.85	3.68E−1	6.10E−2	1.09E−2	2.10E−3	4.25E−4	9.90 E−5			
4.9375	Consistent tangent	1.86	2.56E−1	4.32E−3	2.87E−5						
5.0	Continuum tangent	3.35	3.50E−1	5.05E−2	8.31E−3	1.32E−3	2.32 E−4	5.33 E−5			
7.0625	Consistent tangent	13.8	2.41	3.06E−1	2.44E−4	3.35E−5					
7.1875	Continunm tangent	7.86	1.41	3.17E−1	7.67E−2	2.02E−2	5.73 E−3	1.73 E−3	5.45E−4	1.82E−4	7.02E−5
9.125	Consistent tangent	13.0	1.94	5.97E−1	4.94E−3	3.18E−5					
9.0625	Continunm tangent	8.01	1.40	2.99E−1	6.69E−2	1.73E−2	4.90 E−3	1.49 E−3	4.75E−4	1.61E−4	6.41E−5

6 Conclusions

For nonlinear mechanics problems involving rate constitutive equations, such as rate-independent elasto-plasticity, consistent (or algorithmic) tangent moduli play an important role in guaranteeing the quadratic rate of asymptotic convergence of incremental-iterative solution schemes based on Newton's method. Furthermore, consistent tangent moduli are necessary in structural response sensitivity analysis based on the DDM.

In this paper, the consistent tangent moduli are derived for the multi-axial, multi-yield J_2 (von Mises) plasticity model, a very versatile material constitutive model used extensively in geotechnical engineering. The derived consistent tangent moduli and their software implementation in a nonlinear structural/geotechnical analysis framework are verified through two application examples, one with quasi-static loading and the other with dynamic loading. In the context of these examples, comparative studies are performed between the use of continuum and consistent tangent moduli in terms of convergence rate and computational time of Newton's process. Based on the results obtained for these two examples, the following conclusions can be drawn:

1. For a relatively large (loose) convergence tolerance, Newton's process converges slightly faster when using the consistent over the continuum tangent moduli. However, this does not ensure a reduction in computational time (as compared when using the continuum tangent moduli), since at each iteration of each load/time step, more computational work is required to form the consistent tangent moduli than to form the continuum tangent moduli.
2. As the convergence tolerance is tightened (decreased), use of the consistent tangent moduli reduces significantly (as compared when using the continuum tangent moduli) both the number of iterations per load/time step and the computational time of Newton's process. When using the consistent tangent moduli, the decreasing norm of the unbalanced force vector follows the asymptotic rate of quadratic convergence characteristic of Newton's process.
3. In dynamic analysis and for relatively large time step size, the use of the consistent tangent moduli reduces significantly both the number of iterations per time step and the computational time, even for relatively large convergence tolerance.
4. Increasing the number of yield surfaces in the multi-yield J_2 plasticity model has negligible effect on the comparative results between the uses of consistent and continuum tangent moduli when considering the convergence rate and computational time.
5. In some cases, the use of the consistent tangent moduli alleviates convergence problems (in the Newton iterative process) encountered when using the continuum tangent moduli.

Acknowledgments This research was partially funded by the Pacific Earthquake Engineering Research (PEER) Center through the Earthquake Engineering Research Center Program of the National Science Foundation under Award No. EEC-9701568 and a grant from Lawrence Livermore National Laboratory with Dr. David McCallen as Program Leader. This support is gratefully acknowledged. The authors would like to thank Dr. Jinchi Lu for providing invaluable help for the use of the OpenSeesPL software to create the mesh for third application example. Any opinions, findings, conclusions, or recommendations expressed in this publication are those of the authors and do not necessarily reflect the views of the sponsor.

Appendix A: Derivations of plastic stress correction

This appendix provides the derivation of Eqs. (13) and (19) based on the flowchart of the integration algorithm for the multi-yield surface J_2 plasticity model by Prevost [29]. Although not the focus of this paper, these derivations provide insight into this model. It is worthy to note that the plastic stress correction tensor used in the discretized flow rule (i.e., P1 and P i in Eqs. (13) and (19)) is derived independently by the authors and after some simplifications and approximations reduces to the same form as the one given by Parra [30] and Yang [14] (i.e., Eqs. (13) and (19)) and implemented in OpenSees.

A.1 Derivation of stress correction for the first crossed yield surface

The stress correction for the first crossed yield surface is similar to that for classical J_2 single surface plasticity. The stress correction computation is based on the following two sets of discretized relations.

(a) Incremental stress–strain relation

In small strain plasticity, the decomposition of the total strain into the elastic and plastic parts can be expressed in discretized form as $\Delta\boldsymbol{\varepsilon} = \Delta\boldsymbol{\varepsilon}^{\mathrm{e}} + \Delta\boldsymbol{\varepsilon}^{\mathrm{p}} = \Delta\boldsymbol{\varepsilon}^{\mathrm{e}} + \Delta e^{\mathrm{p}}$. The equality $\Delta\boldsymbol{\varepsilon}^{\mathrm{p}} = \Delta e^{\mathrm{p}}$ stems from the pressure invariant nature of the plasticity model considered here (i.e., isochoric plastic deformations). The incremental stress–strain relation for linear elastic isotropic material can be expressed as

$$\begin{aligned}\boldsymbol{\tau} - \boldsymbol{\tau}_{\mathrm{n}} = \Delta\boldsymbol{\tau} &= \left[\mathbf{C} : \Delta\boldsymbol{\varepsilon}^{\mathrm{e}}\right]^{\mathrm{dev}} = \left[\mathbf{C} : \left(\Delta\boldsymbol{\varepsilon} - \Delta\boldsymbol{\varepsilon}^{\mathrm{p}}\right)\right]^{\mathrm{dev}} \\ &= 2\mathrm{G}\left([\Delta\boldsymbol{\varepsilon}]^{\mathrm{dev}} - \Delta\mathbf{e}^{\mathrm{p}}\right)\end{aligned} \tag{A1}$$

where $\boldsymbol{\tau}_n$ represents the deviatoric stress at the last converged load/time step and the superscript $[\ldots]^{dev}$ denotes the deviatoric part of the quantity inside the brackets. The tensor of elastic moduli $\mathbf{C}$ can be expressed as $\mathbf{C} = \lambda\mathbf{I} \otimes \mathbf{I} + 2G\mathbf{I}_4$. Equation (A1) can be rewritten as

$$\begin{aligned}\boldsymbol{\tau} &= \boldsymbol{\tau}_n + \Delta\boldsymbol{\tau} = \boldsymbol{\tau}_n + 2G\,[\Delta\boldsymbol{\varepsilon}]^{dev} - 2G\Delta\mathbf{e}^p \\ &= \boldsymbol{\tau}_0^{tr} - 2G\Delta\mathbf{e}^p \end{aligned} \tag{A2}$$

Defining the plastic stress correction tensor as (see Fig. 2)

$$\mathbf{P}_1 = 2G\Delta\mathbf{e}^p \tag{A3}$$

the current deviatoric stress can be expressed as

$$\boldsymbol{\tau} = \boldsymbol{\tau}_0^{tr} - \mathbf{P}_1 = \boldsymbol{\tau}_1^{tr} \tag{A4}$$

(b) Discretized form of flow rule

In incremental form, the continuum flow rule in Eqs. (5) and (7) becomes

$$\Delta\mathbf{e}^p = \frac{\langle L\rangle}{H'^{(m)}}\mathbf{Q}_1 = \frac{\langle \mathbf{Q}_1 : \Delta\boldsymbol{\tau}\rangle}{H'^{(m)}}\mathbf{Q}_1 \tag{A5}$$

where $H'^{(m)}$ is the plastic shear modulus of the current (or active) yield surface. The plastic strain increment tensor in Eq. (A5) must obey the Kuhn–Tucker complementarity conditions expressed as $\frac{\langle L\rangle}{H'^{(m)}} f_m(\boldsymbol{\tau}, \boldsymbol{\alpha}) = 0$ where $L = \mathbf{Q}_1 : \Delta\boldsymbol{\tau}$. It can be shown that at the end of the first iterative correction, $\langle \mathbf{Q}_1 : \Delta\tau\rangle$ can be replaced by $\langle \mathbf{Q}_1 : (\boldsymbol{\tau} - \boldsymbol{\tau}_A)\rangle$ where $\boldsymbol{\tau}_A$ is the intersection of $(\boldsymbol{\tau}_0^{tr} - \boldsymbol{\tau}_n)$ with the yield surface $\{f_m = 0\}$ (see Fig. 2). In addition, for the current plastic loading case, $\langle \mathbf{Q}_1 : (\boldsymbol{\tau} - \boldsymbol{\tau}_A)\rangle$ can be approximated by $\mathbf{Q}_1 : (\boldsymbol{\tau} - \boldsymbol{\tau}_1^*)$. Thus, Eq. (A5) becomes

$$\Delta\mathbf{e}^p = \frac{1}{H'^{(m)}}\mathbf{Q}_1 \otimes \mathbf{Q}_1 : \left(\boldsymbol{\tau} - \boldsymbol{\tau}_1^*\right) \tag{A6}$$

Solving Eqs. (A2) and (A6) for the total plastic strain increment $\Delta\mathbf{e}^p$ yields

$$\Delta\mathbf{e}^p = \frac{\mathbf{Q}_1 : \left(\boldsymbol{\tau}_0^{tr} - \boldsymbol{\tau}_1^*\right)}{H'^{(m)} + 2G}\mathbf{Q}_1 \tag{A7}$$

Then, from Eq. (A3)

$$\mathbf{P}_1 = 2G\Delta\mathbf{e}^p = 2G\frac{\mathbf{Q}_1 : \left(\boldsymbol{\tau}_0^{tr} - \boldsymbol{\tau}_1^*\right)}{\left(H'^{(m)} + 2G\right)}\mathbf{Q}_1 \tag{A8}$$

A.2 Derivation of stress correction for the second and successive crossed yield surfaces

After completion of the stress correction for the first yield surface, if the stress point lies outside the next larger yield surface, then before continuing the stress correction corresponding to the next yield surface, some small but crucial correction to the stress $\boldsymbol{\tau}_1^{tr}$ must be made in order to account for the fact that the plastic stress correction has actually been 'overrelaxed' at the first stress correction step [29].

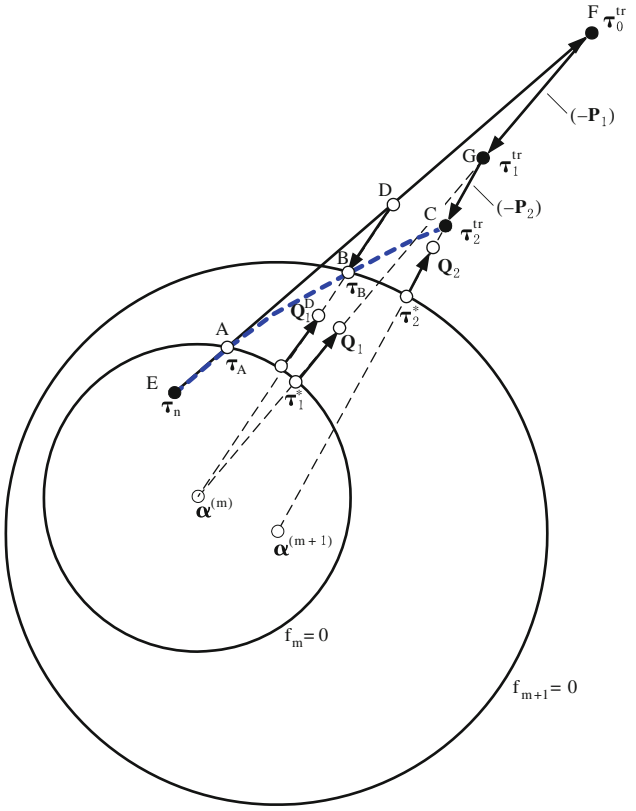

Fig. 43 Flow rule of multi-yield-surface J_2 plasticity model

The total deviatoric strain increment $[\Delta\boldsymbol{\varepsilon}]^{dev}$ may be subdivided into three parts (E–A, A–B, and B–C, see Fig. 43), where E is the stress point $\boldsymbol{\tau}_n$ at the last converged time/load step. Stress path E–A is linear elastic, i.e, $f_m \leq 0$ and the equality holds only at point A. A–B is the path of the stress state between the first yield surface ($f_m = 0$) and the second yield surface ($f_{m+1} = 0$). Stress point B may be obtained by the 'elastic predictor A–D, plastic corrector D–B' process and by satisfying the consistency condition $f_{m+1} = 0$. The exact position of point B could be obtained iteratively.

The entire elastic predictor E–F has been relaxed plastically to stress point $\boldsymbol{\tau}_1^{tr}$ (point G in Fig. 43) according to the first yield surface ($f_m = 0$) only. The portion D-F of the elastic predictor E–F should be relaxed plastically according to the second yield surface ($f_{m+1} = 0$). Thus, the plastic stress correction F–G $(-\mathbf{P}_1)$ must be scaled back to F–H (see Fig. 44) where the deviatoric plastic strain at point H is the same as at point B (i.e., $\mathbf{e}_H^p = \mathbf{e}_B^p$). Then, the plastic stress correction F–H is followed by the plastic stress correction H–I according to the second yield surface ($f_{m+1} = 0$) resulting in stress state$\boldsymbol{\tau}_2^{tr}$. The plastic strain from stress point G to stress point I can be decomposed as (see Fig. 44)

$$\Delta\boldsymbol{\varepsilon}_{GI}^p = -\Delta\boldsymbol{\varepsilon}_{HG}^p + \Delta\boldsymbol{\varepsilon}_{HI}^p \tag{A9}$$

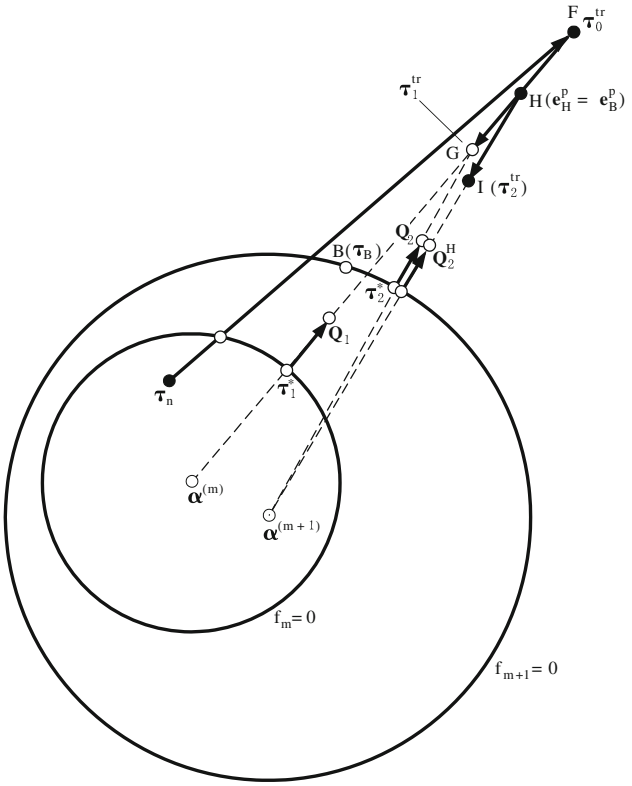

Fig. 44 Flow rule of multi-yield-surface J_2 plasticity model

Note that both $\Delta\boldsymbol{\varepsilon}^{\mathrm{p}}_{\mathrm{HG}}$ and $\Delta\boldsymbol{\varepsilon}^{\mathrm{p}}_{\mathrm{HI}}$ correspond to the plastic loading case. The second stress correction $(-\mathbf{P}_2)$ is obtained from the following two sets of discretized relations.

(a) Incremental stress–strain relation (from $G(\boldsymbol{\tau}_1^{\mathrm{tr}})$ to $I(\boldsymbol{\tau}_2^{\mathrm{tr}})$)

Since, between stress points G and I (see Fig. 44), the total strain remains unchanged, i.e., $\Delta\boldsymbol{\varepsilon}_{\mathrm{GI}} = 0$, it follows that

$$\begin{aligned}\boldsymbol{\tau}_2^{\mathrm{tr}} - \boldsymbol{\tau}_1^{\mathrm{tr}} &= \mathbf{C} : \left(\Delta\boldsymbol{\varepsilon}^{\mathrm{e}}_{\mathrm{GI}}\right) = \mathbf{C} : \left(\Delta\boldsymbol{\varepsilon}_{\mathrm{GI}} - \Delta\boldsymbol{\varepsilon}^{\mathrm{p}}_{\mathrm{GI}}\right)\\ &= -\mathbf{C} : \Delta\boldsymbol{\varepsilon}^{\mathrm{p}}_{\mathrm{GI}} = -2\mathrm{G}\Delta\boldsymbol{\varepsilon}^{\mathrm{p}}_{\mathrm{GI}}\end{aligned} \tag{A10}$$

where $\Delta\boldsymbol{\varepsilon}^{\mathrm{p}}_{\mathrm{GI}} = \Delta\mathbf{e}^{\mathrm{p}}_{\mathrm{GI}}$.

(b) Discretized form of flow rule

The plastic strain increment from stress point H to stress point I is given by the plastic strain increment from stress point B to stress point I and defined as, according to Eq. (5),

$$\Delta\boldsymbol{\varepsilon}^{\mathrm{p}}_{\mathrm{HI}} = \frac{\langle \mathrm{L}_2\rangle}{\mathrm{H}'^{(\mathrm{m}+1)}}\mathbf{Q}_2^{\mathrm{H}} = \frac{\left\langle \mathbf{Q}_2^{\mathrm{H}} : \Delta\boldsymbol{\tau}_2\right\rangle}{\mathrm{H}'^{(\mathrm{m}+1)}}\mathbf{Q}_2^{\mathrm{H}} \tag{A11}$$

where $\Delta\boldsymbol{\tau}_2$ is defined as the stress change from B to I (see Fig. 43 and 44). For the plastic loading case, $\left\langle \mathbf{Q}_2^{\mathrm{H}} : \Delta\boldsymbol{\tau}_2\right\rangle$ can be approximated with $\mathbf{Q}_2 : (\boldsymbol{\tau}_2^{\mathrm{tr}} - \boldsymbol{\tau}_2^*)$ (see Fig. 44) in which $\boldsymbol{\tau}_2^*$ and $\mathbf{Q}_2$ are as defined in Eqs. (15) and (17), respectively. Substituting this approximation as well as $\mathbf{Q}_2^{\mathrm{H}} \cong \mathbf{Q}_2$ into Eq. (A11), which in turn is substituted into Eq. (A9), yields

$$\Delta\boldsymbol{\varepsilon}^{\mathrm{p}}_{\mathrm{HI}} = \Delta\boldsymbol{\varepsilon}^{\mathrm{p}}_{\mathrm{HG}} + \Delta\boldsymbol{\varepsilon}^{\mathrm{p}}_{\mathrm{GI}} = \frac{1}{\mathrm{H}'^{(\mathrm{m}+1)}}\mathbf{Q}_2\left(\mathbf{Q}_2 : \left(\boldsymbol{\tau}_2^{\mathrm{tr}} - \boldsymbol{\tau}_2^*\right)\right) \tag{A12}$$

The plastic strain increment $\Delta\boldsymbol{\varepsilon}^{\mathrm{p}}_{\mathrm{HG}}$ corresponding to the stress increment H-G by which the stress state was over relaxed (according to the first yield surface), can be approximated as (see Eq. (5) and Fig. 44)

$$\begin{aligned}\Delta\boldsymbol{\varepsilon}^{\mathrm{p}}_{\mathrm{HG}} &= \frac{1}{\mathrm{H}'^{(\mathrm{m})}}\mathbf{Q}_1\left(\mathbf{Q}_1 : \left(\boldsymbol{\tau}_1^{\mathrm{tr}} - \boldsymbol{\tau}_{\mathrm{B}}\right)\right)\\ &\approx \frac{1}{\mathrm{H}'^{(\mathrm{m})}}\mathbf{Q}_1\left(\mathbf{Q}_1 : \left(\boldsymbol{\tau}_1^{\mathrm{tr}} - \boldsymbol{\tau}_2^*\right)\right)\end{aligned} \tag{A13}$$

Substituting Eq. (A13) into Eq. (A12) gives

$$\begin{aligned}\Delta\boldsymbol{\varepsilon}^{\mathrm{p}}_{\mathrm{GI}} &= \frac{1}{\mathrm{H}'^{(\mathrm{m}+1)}}\mathbf{Q}_2\left(\mathbf{Q}_2 : \left(\boldsymbol{\tau}_2^{\mathrm{tr}} - \boldsymbol{\tau}_2^*\right)\right)\\ &\quad - \frac{1}{\mathrm{H}'^{(\mathrm{m})}}\mathbf{Q}_1\left(\mathbf{Q}_1 : \left(\boldsymbol{\tau}_1^{\mathrm{tr}} - \boldsymbol{\tau}_2^*\right)\right)\end{aligned} \tag{A14}$$

Solving Eqs. (A10) and (A14) for $\boldsymbol{\tau}_2^{\mathrm{tr}}$ and $\Delta\boldsymbol{\varepsilon}^{\mathrm{p}}_{\mathrm{GI}}$, it is found that

$$\begin{aligned}\Delta\boldsymbol{\varepsilon}^{\mathrm{p}}_{\mathrm{GI}} &= \frac{\left(\mathrm{H}'^{(\mathrm{m})} + 2\mathrm{G}\cdot\mathbf{Q}_1 : \mathbf{Q}_2\right)}{\mathrm{H}'^{(\mathrm{m})}\left(\mathrm{H}'^{(\mathrm{m}+1)} + 2\mathrm{G}\right)}\mathbf{Q}_2 \otimes \mathbf{Q}_2 : \left(\boldsymbol{\tau}_1^{\mathrm{tr}} - \boldsymbol{\tau}_2^*\right)\\ &\quad - \frac{1}{\mathrm{H}'^{(\mathrm{m})}}\mathbf{Q}_1 \otimes \mathbf{Q}_1 : \left(\boldsymbol{\tau}_1^{\mathrm{tr}} - \boldsymbol{\tau}_2^*\right)\end{aligned} \tag{A15}$$

The second plastic stress correction $\mathbf{P}_2 = \boldsymbol{\tau}_1^{\mathrm{tr}} - \boldsymbol{\tau}_2^{\mathrm{tr}}$ can then be obtained as

$$\begin{aligned}\mathbf{P}_2 = \mathbf{C} : \Delta\boldsymbol{\varepsilon}^{\mathrm{p}}_{\mathrm{GI}} &= 2\mathrm{G}\frac{\left(\mathrm{H}'^{(\mathrm{m})} + 2\mathrm{G}\cdot\mathbf{Q}_1 : \mathbf{Q}_2\right)}{\mathrm{H}'^{(\mathrm{m})}\left(\mathrm{H}'^{(\mathrm{m}+1)} + 2\mathrm{G}\right)}\mathbf{Q}_2\\ &\quad \otimes \mathbf{Q}_2 : \left(\boldsymbol{\tau}_1^{\mathrm{tr}} - \boldsymbol{\tau}_2^*\right) - \frac{2\mathrm{G}}{\mathrm{H}'^{(\mathrm{m})}}\mathbf{Q}_1 \otimes \mathbf{Q}_1 : \left(\boldsymbol{\tau}_1^{\mathrm{tr}} - \boldsymbol{\tau}_2^*\right)\end{aligned} \tag{A16}$$

After the second plastic stress correction, if the stress lies outside the next yield surface, the correction process from Eq. (A9) to Eq. (A16) is repeated with the subscript for the iteration number set to i = 3. More generally, the plastic stress correction for iteration i (corresponding to yield surface $\mathrm{f}_{\mathrm{m}+\mathrm{i}-1} = 0$) is given by

$$\begin{aligned}\mathbf{P}_{\mathrm{i}} &= 2\mathrm{G}\frac{\left(\mathrm{H}'^{(\mathrm{m}+\mathrm{i}-2)} + 2\mathrm{G}\cdot\mathbf{Q}_{\mathrm{i}-1} : \mathbf{Q}_{\mathrm{i}}\right)}{\mathrm{H}'^{(\mathrm{m}+\mathrm{i}-2)}\left(\mathrm{H}'^{(\mathrm{m}+\mathrm{i}-1)} + 2\mathrm{G}\right)}\\ &\quad \times\mathbf{Q}_{\mathrm{i}} \otimes \mathbf{Q}_{\mathrm{i}} : \left(\boldsymbol{\tau}_{\mathrm{i}-1}^{\mathrm{tr}} - \boldsymbol{\tau}_{\mathrm{i}}^*\right)\\ &\quad - \frac{2\mathrm{G}}{\mathrm{H}'^{(\mathrm{m}+\mathrm{i}-2)}}\mathbf{Q}_{\mathrm{i}-1} \otimes \mathbf{Q}_{\mathrm{i}-1} : \left(\boldsymbol{\tau}_{\mathrm{i}-1}^{\mathrm{tr}} - \boldsymbol{\tau}_{\mathrm{i}}^*\right)\end{aligned} \tag{A17}$$

If the number of yield surfaces used to represent the original shear stress–strain backbone curve (see Eq. (2)) is large enough (say NYS > 20) such that the unit tensors normal to the two consecutive yield surfaces $\mathrm{f}_{\mathrm{m}+\mathrm{i}-2} = 0$ and

$f_{m+i-1} = 0$ corresponding to stress points $\boldsymbol{\tau}^{tr}_{i-2}$ and $\boldsymbol{\tau}^{tr}_{i-1}$, respectively, are close, then

$$\mathbf{Q}_{i-1} \approx \mathbf{Q}_i \tag{A18}$$

and Eq. (A17) further simplifies to

$$\begin{aligned}\mathbf{P}_i &= 2G\frac{\left(H'^{(m+i-2)} - H'^{(m+i-1)}\right)}{H'^{(m+i-2)}\left(H'^{(m+i-1)}+2G\right)}\mathbf{Q}_i \otimes \mathbf{Q}_i : \left(\boldsymbol{\tau}^{tr}_{i-1} - \boldsymbol{\tau}^{*}_{i}\right) \\ &= 2G\frac{\mathbf{Q}_i : \left(\boldsymbol{\tau}^{tr}_{i-1} - \boldsymbol{\tau}^{*}_{i}\right)}{\left(H'^{(m+i-1)} + 2G\right)}\frac{\left(H'^{(m+i-2)} - H'^{(m+i-1)}\right)}{H'^{(m+i-2)}}\mathbf{Q}_i\end{aligned} \tag{A19}$$

It is worth mentioning that the "elastic predictor – plastic corrector" constitutive law integration method considered in this paper is an implicit method based on the use of backward Euler method to discretize the continuous flow rule in Eq. (5). However, this method does not require iterations. This is due to (i) the mathematical simplicity of the von Mises yield surfaces used here, and (ii) the piecewise linear approximation of the original smooth (shear stress–strain) backbone curve. The plastic stress corrections (in Eqs. (A8) and (A19)) corresponding to each active yield surface can be solved non-iteratively as shown in Appendix A. Therefore, the stress at the current time step n + 1 may be obtained non-iteratively (i.e., using Eqs. (8) through (22)).

References

1. Simo JC, Taylor RL (1985) Consistent tangent operators for rate-independent elastoplasticity. Comput Methods Appl Mech Eng 48:101–118
2. Simo JC, Hughes TJR (1998) Computational inelasticity. Springer, Berlin
3. Kleiber M, Antunez H, Kowalczyk P (1997) Parameter sensitivity in nonlinear mechanics: theory and finite element computations. Wiley, New York
4. Conte JP, Vijalapura PK, Meghella M (2003) Consistent finite element response sensitivity analysis. J Eng Mech (ASCE) 129(12):1380–1393
5. Conte JP, Barbato M, Spacone E (2004) Finite element response sensitivity analysis using force-based frame models. Int J Numer Methods Eng 59:1781–1820
6. Iwan WD (1967) On a class of models for the yielding behavior of continuous and composite systems. J Appl Mech Trans (ASME) 34(E3):612–617
7. Mroz Z (1967) On the description of anisotropic workhardening. J Mech Phys Solids 15:163–175
8. Prevost JH (1977) Mathematical modelling of monotonic and cyclic undrained clay behaviour. Int J Numer Anal Methods Geomech 1(2):195–216
9. Prevost JH (1978) Plasticity theory for soil stress-strain behavior. J Eng Mech Div (ASCE) 104(EM5):1177–1194
10. Prevost JH (1978) Anisotropic undrained stress-strain behavior of clays. J Geotech Eng Div (ASCE) 104(GT8):1075–1090
11. Elgamal A, Yang Z, Parra E, Ragheb A (2003) Modeling of cyclic mobility in saturated cohesionless soils. Int J Plasticity 19:883–905. http://cyclic.ucsd.edu
12. Mazzoni S, McKenna F, Fenves GL (2006) Open system for earthquake engineering simulation user manual (Version 1.6.2). Pacific Earthquake Engineering Research Center, University of California, Berkeley, California. http://opensees.berkeley.edu/OpenSees/manuals/usermanual
13. Zhang Y, Conte JP, Yang Z, Elgamal A, Bielak J, Acero G (2008) Two-dimensional nonlinear earthquake response analysis of a bridge-foundation-ground system. Earthq Spectra 24(2):343–386
14. Yang Z (2000) Numerical modeling of earthquake site response including dilation and liquefaction. PhD Dissertation, Department of Civil Engineering and Engineering Mechanics, Columbia University, New York
15. Chen WF, Mizuno E (1990) Nonlinear analysis in soil mechanics—theory and implementation. Elsevier, Amsterdam
16. Prevost JH, Abdel-Ghaffar AM, Elgamal A (1985) Nonlinear hysteretic dynamic response of soil systems. J Eng Mech Div (ASCE) 111(EM5):696–713
17. Abdel-Ghaffar AM, Elgamal A (1987) Elasto-plastic earthquake-response of 3-D non-homogeneous earth dams: theory. J Geotech Eng Div (ASCE) 113(GT11):1293–1308
18. Elgamal A, Abdel-Ghaffar AM (1987) Elasto-plastic seismic-response of 3-D earth dams: application. J Geotech Eng Div (ASCE) 113(GT11):1309–1325
19. Elgamal A (1992) Three dimensional seismic analysis of La Villita dam. J Geotech Eng Div (ASCE) 118(GT12):1937–1958
20. Elgamal A, Gunturi V (1993) Dynamic behavior and seismic response of El Infiernillo dam. J Earthq Eng Struct Dyn 22(8):665–684
21. Elgamal A, Zeghal M, Parra E, Gunturi R, Tang HT, Stepp JC (1996) Identification and modeling of earthquake ground response: site amplification. Soil Dyn Earthq Eng 15:499–522
22. Elgamal A, Lai T, Yang Z, He L (2001) Dynamic soil properties. Seismic downhole arrays and applications in practice. In: Prakash S (ed) 4th International conference on recent advances in geotechnical earthquake engineering and soil dynamics, San Diego, California, USA, March 26–31, 2001
23. Elgamal A, Yan L, Yang Z, Conte JP (2008) Three-dimensional seismic response of Humboldt Bay bridge-foundation ground system. J Struct Eng (ASCE) 134(7):1165–1176
24. Gu Q, Conte JP, Elgamal A, Yang Z (2009) Finite element response sensitivity analysis of multi-yield-surface J_2 plasticity model by direct differentiation method. Comput Methods Appl Mech Eng 198(30–32):2272–2285
25. Ditlevsen O, Madsen HO (1996) Structural reliability methods. Wiley, New York
26. Montans FJ (2000) Implicit algorithms for multilayer J_2-plasticity. Comput Methods Appl Mech Eng 189:673–700
27. Manzari MT, Prachathananukit R (2001) On integration of a cyclic soil plasticity model. Int J Numer Anal Methods Geomech 25:525–549
28. Simo JC, Kennedy JG, Govindjee S (2005) Non-smooth multisurface plasticity and viscoplasticity. Loading/unloading conditions and numerical algorithms. Int J Numer Methods Eng 26(10):2161–2185
29. Prevost JH (1989) DYNA1D: a computer program for nonlinear seismic site response analysis—technical documentation. Technical Report NCEER-89-0025, National Center for Earthquake Engineering Research, State University of New York, Red Jacket Quadrangle, Buffalo, NY 14261, USA
30. Parra E (1996) Numerical modeling of liquefaction and lateral ground deformation including cyclic mobility and dilative behavior in soil systems. PhD dissertation, Department of Civil Engineering, Rensselaer Polytechnic Institute
31. Kramer SL (1996) Geotechnical earthquake engineering. Prentice-Hall, Upper Saddle River

32. Kondner RL (1963) Hyperbolic stress-strain response: cohesive soils. J Soil Mech Found Div (ASCE) 89(SM1):115–143
33. Yang Z, Elgamal A, Parra E (2003) Computational model for cyclic mobility and associated shear deformation. J Geotech Geoenviron Eng 129(12):1119–1127
34. Elgamal A (2002) Constitutive modeling and numerical implementation. Lecture notes, Department of Structural Engineering, University of California at San Diego, La Jolla, CA 92093, USA
35. Haftka RT, Gurdal Z (1993) Elements of structural optimization. Kluwer, Dordrecht
36. Helnwein P (2001) Some remarks on the compressed matrix representation of symmetric second-order and fourth-order tensors. Comput Methods Appl Mech Eng 190(22–23):2753–2770
37. Elgamal A, Yang Z, Lai T, Kutter BL, Wilson DJ (2005) Dynamic response of saturated dense sand in laminated centrifuge container. Geotech Geoenviron Eng (ASCE) 131(5):598–609
38. Elgamal A, Lu J (2009) A framework for 3D finite element analysis of lateral pile system response. Contemporary topics in in site testing, analysis, and reliability of foundations. ASCE Geotechnical Special Publication, vol 186, pp 616–623. http://cyclic.ucsd.edu/openseespl/